https://doi.org/10.5194/egusphere-2026-4663
Preprint. Discussion started: 10 August 2026


# Global Sampling Characteristics and Coverage Complementarity of 12 GNSS Radio Occultation Constellations

Wenqiang Lu[1,2,3*], Ran Chen[4,5*], Na Xu[1,2,3], Xiangguang Meng[4,5], Lei Xue[6], Mi Liao[1,2,3], Yan Liu[7], Peng Guo[8], Guanglin Yang[1,2,3], Xiuqing Hu[1,2,3], Xiangang Zhao[1,2,3], Yueqiang Sun[4,5]

[1]National Satellite Meteorological Center/National Center for Space Weather, Beijing 100081, China
[2]Innovation Center for Fengyun Meteorological Satellite (FYSIC), Beijing 100081, China
[3]Key Laboratory of Radiometric Calibration and Validation for Environmental Satellites, CMA, Beijing 100081, China
[4]National Space Science Center, Chinese Academy of Sciences, Beijing 100190, China
[5]College of Earth and Planetary Sciences, University of Chinese Academy of Sciences, Beijing 100049, China
[6]National Meteorological Information Center, China Meteorological Administration, Beijing 100081, China
[7]Earth System Modeling and Prediction Center, China Meteorological Administration, Beijing 100081, China
[8]Shanghai Astronomical Observatory, Chinese Academy of Sciences, Shanghai 200030, China

* These authors contributed equally to this work.

*Correspondence to*: Na Xu(xuna@cma.gov.cn), Xiangguang Meng(xgmeng@nssc.ac.cn)

**Abstract.** This study uses observations from COSMIC-2, FY-3, GRACE-C/D, KOMPSAT-5, MetOp-A/C, PAZ, PlanetiQ, Sentinel-6A, Spire, TerraSAR-X/TanDEM-X, TM-1, and YY-1 during 1–7 January 2026 to compare their spatial distributions, grid coverage, local-time sampling, and retrieval accuracy; it also assesses the benefits of multi-mission integration and the potential effects of COSMIC-2 retirement on the integrated observing capability. The results show that orbital configuration determines latitudinal and local-time sampling, whereas event abundance and constellation size primarily control grid coverage. Large constellations such as YY-1 and TM-1 provide the strongest global continuity, while missions with different orbital inclinations offer complementary sampling across latitude bands. Combining all missions substantially reduces spatial gaps and provides near-global coverage at 1.0° and 2.0° resolutions. Within 6 h windows, joint coverage reaches 70.98% at 2.0° resolution. The combined observations also broaden local-time sampling, whereas COSMIC-2 remains particularly important for equatorial coverage. Therefore, the retirement of COSMIC-2 would reduce equatorial sampling capability and should be considered in the development of future multi-mission GNSS-RO observing systems. Comparisons with ERA5 indicate broadly consistent retrieval accuracy among most missions between 10 and 35 km, with larger differences in the lower troposphere. These findings demonstrate the value of integrating missions with diverse orbital configurations and highlight the need to sustain complementary sampling after the retirement of key missions.

## 1 Introduction

Global navigation satellite system (GNSS) radio occultation (RO) is a space-based sounding technique that uses the refraction, bending, and propagation delay experienced by GNSS signals as they traverse the Earth's atmosphere and ionosphere. These measurements are inverted to obtain vertical profiles of atmospheric refractivity and, subsequently, key

https://doi.org/10.5194/egusphere-2026-4663
Preprint. Discussion started: 10 August 2026


physical parameters such as temperature, pressure, water vapor, and ionospheric electron density (Kursinski et al., 1997). GNSS-RO measurements rely on precise timing and phase observations and are only weakly affected by clouds and precipitation. The technique therefore provides all-weather global coverage, high vertical resolution, and strong long-term stability, making it valuable for numerical weather prediction, climate monitoring, and space-weather research (Ho et al., 2012).

GNSS-RO originated with the GPS/MET demonstration mission in the late twentieth century. During its operation, GPS/MET acquired extensive observations and successfully retrieved neutral-atmosphere profiles from 0 to 60 km, demonstrating the feasibility of GNSS-RO atmospheric sounding (Rocken et al., 1997). Subsequent single-satellite missions, including CHAMP (Wickert et al., 2001) and GRACE (Beyerle et al., 2005), advanced RO data processing, retrieval algorithms, and applications. The six-satellite COSMIC-1 constellation, launched in 2006, enabled the first large-scale operational use of GNSS-RO observations and substantially increased the number of global RO profiles, marking an important transition from technology demonstration to operational application (Anthes et al., 2008). Later missions, including the MetOp series (Bonnedal et al., 2010), the FY-3 series (Bai et al., 2014) COSMIC-2 (Schreiner et al., 2020), and Sentinel-6/Jason-CS (Donlon et al., 2021), have provided stable observations and broadened the use of GNSS-RO in numerical weather prediction, climate monitoring, and space-weather research. More recently, low-Earth-orbit small-satellite constellations and commercial missions such as Spire, PlanetiQ, TM-1, and YY-1 have further increased the number and spatial sampling density of RO events, creating a multi-source observing system that combines demonstration missions, operational meteorological satellites, and commercial constellations.

Advances in low-Earth-orbit platforms, spaceborne GNSS receivers, and RO retrieval techniques have transformed GNSS-RO from a small number of demonstration missions into a global system of concurrent missions and constellations. Differences in orbital altitude, inclination, local-time configuration, constellation size, and received signal systems produce distinct global distributions, latitudinal coverage patterns, local-time sampling, and observation densities. Low-inclination missions generally enhance sampling at low and middle latitudes, high-inclination or near-polar missions improve middle- and high-latitude coverage, and large or commercial constellations improve global coverage continuity through higher observation frequencies.

For global atmospheric monitoring and data assimilation, the value of RO data depends not only on the retrieval accuracy of individual profiles but also on the spatiotemporal distribution of the observations. Insufficient sampling within particular latitude bands, local-time intervals, or spatial grids can reduce the representativeness of a mission for weather systems, climate background states, and regional atmospheric structures. Compared with a single mission, joint multi-mission observations exploit complementary orbital configurations to reduce spatial gaps, improve uneven local-time sampling, and increase the continuity and stability of global RO observations. A systematic assessment of individual and combined missions in terms of spatial coverage, grid density, and local-time distribution is therefore important.

This study examines major global GNSS-RO missions, including COSMIC-2, FY-3, GRACE-C/D, KOMPSAT-5, MetOp-A/C, PAZ, PlanetiQ, Sentinel-6A, Spire, TerraSAR-X/TanDEM-X, TM-1, and YY-1. Using RO observations during 1–7

January 2026, we analyze their global spatial distributions, grid-based coverage characteristics, and local-time sampling patterns, and evaluate the improvement in global coverage obtained through multi-mission combinations. Bending-angle and refractivity retrievals are also compared with ERA5 reanalysis fields to support the coordinated use and quality assessment of multi-source GNSS-RO data.

## 2 Missions and data

### 2.1 GNSS-RO missions

To place the missions within the global observing system, Fig. 1 summarizes the development of GNSS-RO from GPS/MET technology demonstration, through single-satellite and operational constellation missions, to the expansion of commercial constellations. Overall, GNSS-RO has evolved from technology demonstration to operational application and from a small number of individual satellites to coordinated multi-constellation observations.

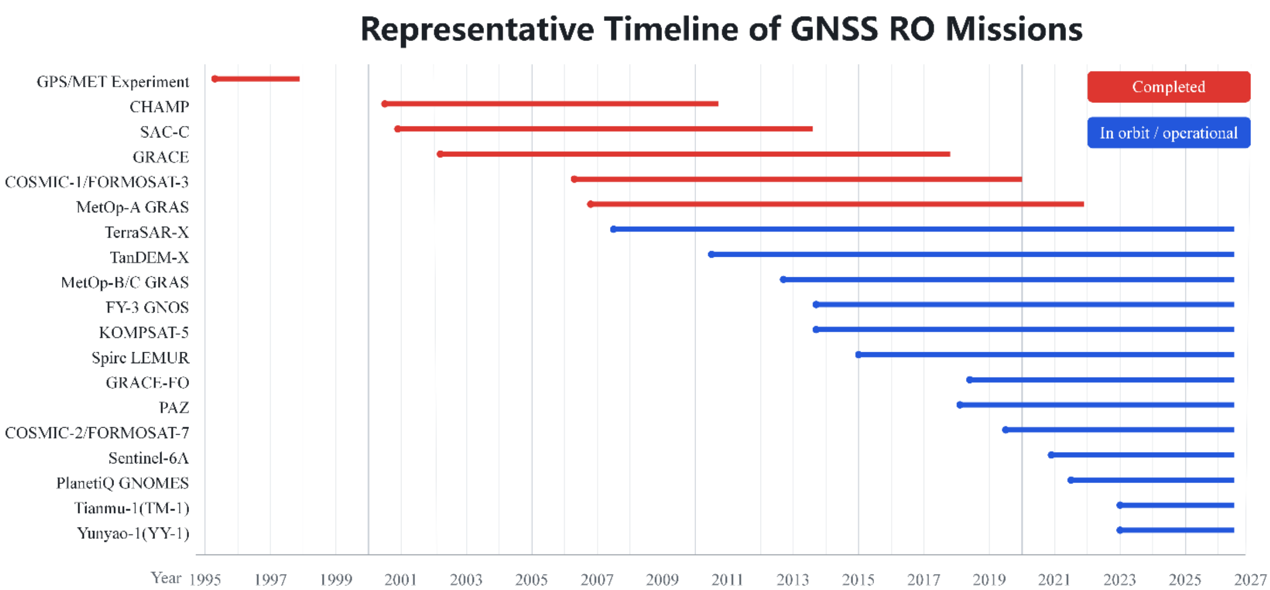


**Figure 1. Development timeline of representative GNSS radio occultation missions.**

COSMIC-2 (Constellation Observing System for Meteorology, Ionosphere and Climate-2) is a next-generation operational GNSS-RO constellation jointly implemented by the United States National Oceanic and Atmospheric Administration and Taiwan. It comprises six low-Earth-orbit satellites launched in June 2019. COSMIC-2 operates in low-inclination, near-circular, non-sun-synchronous orbits at approximately 520-550 km and an inclination of approximately 24 degrees, primarily

https://doi.org/10.5194/egusphere-2026-4663
Preprint. Discussion started: 10 August 2026


covering equatorial and low-latitude regions (Jaeggi et al., 2021). Its receivers support multi-frequency GNSS RO observations (L1, L2, and L5), and each satellite can acquire more than one thousand RO events per day.

Fengyun-3 (FY-3) is China's operational polar-orbiting meteorological satellite series and has carried the GNSS Occultation Sounder (GNOS) since FY-3C (Bai et al., 2014). FY-3D (Du et al., 2019), FY-3E, FY-3F (Miao et al., 2025), and FY-3G (Zhang et al., 2023) occupy different local-time orbits: FY-3E is in a dawn-dusk orbit, FY-3F in a morning orbit, FY-3D in an afternoon orbit, and FY-3G in a low-inclination precipitation-monitoring orbit. Most FY-3 satellites have inclinations near 98 degrees, whereas FY-3G has an inclination near 50 degrees. Their coordinated operation forms the core of China's operational RO observing system.

The twin-satellite GRACE mission was launched in 2002 primarily to observe the Earth's gravity field and also carried GNSS receivers for RO observations. The satellites operated in near-polar orbits at approximately 500 km and an inclination of approximately 89 degrees. GRACE RO data contributed to early studies of atmospheric structure and retrieval algorithms (Beyerle et al., 2005). The follow-on GRACE-C/D twin-satellite mission primarily measures static and time-variable gravity fields while continuing GPS RO observations. GF1 and GF2 have provided approximately 500 atmospheric profiles per day since March 2020 and September 2021, respectively, for climate research and numerical weather prediction (Kornfeld et al., 2019; Schmidt et al., 2020).

KOMPSAT-5 is a Korean multipurpose satellite launched in 2013. Although its primary payload is synthetic aperture radar (SAR), it also supports GNSS-RO and precise orbit determination. It operates in a near-polar, sun-synchronous orbit at an altitude of approximately 550 km (Roh and Hwang, 2020).

MetOp-02 (MetOp-A), MetOp-01 (MetOp-B), and MetOp-03 (MetOp-C) were the three first-generation satellites of the EUMETSAT Polar System (EPS). They were launched on 19 October 2006, 17 September 2012, and 7 November 2018, respectively. All three satellites were placed in near-circular, sun-synchronous polar orbits at an altitude of approximately 817 km and an inclination of approximately 98.7°. Their nominal mid-morning orbit configuration had descending-node and ascending-node local times of approximately 09:30 and 21:30, respectively. Each satellite was equipped with the GNSS Receiver for Atmospheric Sounding (GRAS), which receives dual-frequency GPS L1/L2 signals and retrieves vertical profiles of atmospheric refractivity, temperature, humidity, and ionospheric electron density (Righetti et al., 2020). MetOp-A was retired in November 2021; therefore, only MetOp-B and MetOp-C were operational during the study period in January 2026.

PAZ (SEOSAR/Paz) is an X-band SAR Earth-observation satellite operated by the Spanish company Hisdesat. It was launched from Vandenberg Air Force Base on a SpaceX Falcon 9 rocket on 22 February 2018. PAZ operates in a sun-synchronous low-Earth orbit at approximately 514 km, with an inclination of approximately 97.44 degrees and an approximately 11-day repeat cycle. It flies in coordination with TerraSAR-X and TanDEM-X to enhance revisit capability. Its ascending-node equator-crossing local time is approximately 18:00 ± 0.25 h (Padullés et al., 2024).

PlanetiQ is a US commercial remote-sensing company. Its GNSS-RO satellites are typically deployed in sun-synchronous orbits at approximately 620-645 km, with inclinations near 97.8 degrees and orbital periods near 97 min. The typical

https://doi.org/10.5194/egusphere-2026-4663
Preprint. Discussion started: 10 August 2026


equator-crossing local times are approximately 06:00/18:00, providing stable solar illumination geometry (Zhran et al., 2024).

Sentinel-6A is a joint European-US operational altimetry satellite launched in 2020 and equipped with a GNSS-RO receiver. Its non-sun-synchronous orbit has an inclination of approximately 66 degrees and provides complementary observations at low and middle latitudes (Paolella et al., 2025).

Spire Global operates a commercial constellation that collects GNSS-RO and GNSS reflectometry data using numerous LEMUR nanosatellites. More than one hundred satellites have been launched, forming one of the world's largest commercial GNSS-RO constellations. The satellites occupy multiple low-Earth-orbit planes, including several sun-synchronous planes, at altitudes of approximately 385-650 km. Orbital inclination and local solar time vary among launch batches (Masters et al., 2020).

TerraSAR-X and TanDEM-X are German twin SAR missions that also support GNSS-RO and precise orbit determination. They operate in near-polar, sun-synchronous orbits with an inclination of approximately 97.44 degrees and a designed descending-node local time of 06:00 (Faller et al., 2007).

Tianmu-1 (TM-1) is China's first commercial GNSS-RO meteorological constellation. It comprises multiple networked small satellites in low-Earth orbit at approximately 520 km and an inclination near 97 degrees. The receivers support GPS, BDS, Galileo, and GLONASS signals, substantially increasing global RO observation density (Li et al., 2025).

Yunyao-1 (YY-1) is an important component of China's new generation of commercial GNSS-RO constellations. The planned system comprises 90 satellites equipped with GNSS-RO instruments by the end of 2026 (Fu and Li, 2021). Its design combines 12 high-inclination orbital planes with six satellites per plane and six low-inclination planes with three satellites per plane. The constellation includes quasi-sun-synchronous orbits near 97 degrees and low-inclination orbits near 50 degrees at an altitude of approximately 500 km. This combination of orbital configurations further enhances coverage (Xu et al., 2025).

To keep figure legends concise and clear, standardized abbreviations are used for several missions. Table 1 lists the full mission names and abbreviations used in this study.

**Table 1. GNSS-RO mission names and abbreviations used in this study.**

| **RO Constellation** | **RO Acronym** | **Specific Satellite (Data Directory)** | **RO Constellation** | **RO Acronym** | **Specific Satellite (Data Directory)** |
|---|---|---|---|---|---|
| **COSMIC-2** | **COSMIC-2** | C2E1、C2E2、C2E4、C2E5、C2E6 | **FengYun-3** | **FY-3** | FY3D、FY3E、FY3F、FY3G |
| **GRACE-C/D** | **GRACE** | GRACE-C、GRACE-D | KOMPSAT-5 | **KOM5** | KOM5 |
| **MetOp** | **MetOp** | MetOp01、 | **PAZ** | **PAZ1** | PAZ1 |

https://doi.org/10.5194/egusphere-2026-4663
Preprint. Discussion started: 10 August 2026


| | | | | | |
|---|---|---|---|---|---|
| | | MetOp 03 | | | |
| PlanetiQ | **PLAQ** | PLAQ | Sentinel-6A | **SE6A** | SE6A |
| **SPIRE** | **SPIRE** | **SPIRE** | **TerraSAR-X/TanDEM-X** | **TSX_TDX** | TSAR、TDMX |
| **Tianmu-1** | **TM-1** | TM01–TM22 | **Yunyao-1** | **YY-1** | Y014–Y022、Y025、Y026、Y031–Y040、Y043–Y048、Y055–Y060 |

### 2.2 Data sources

This study used GNSS radio occultation (GNSS-RO) observations from 12 global systems during 1–7 January 2026. The data were obtained from the National Meteorological Information Center (NMIC) in BUFR format and included observations disseminated through the Global Telecommunication System (GTS) and operational products authorized by the China Meteorological Administration from Tianmu and Yunyao companies. The dataset comprised observations from COSMIC-2, FY-3, GRACE-C/D, KOMPSAT-5, MetOp-A/C, PAZ, PlanetiQ, Sentinel-6A, Spire, TerraSAR-X/TanDEM-X, TM-1, and YY-1. It should be noted that the occultation data analyzed in this study represent only the observations accessible through the two aforementioned data channels. The BUFR records include bending angle, impact parameter, occultation tangent-point location, observation time, refractivity, and geometric height. Event latitude, longitude, time, and mission identifier were extracted to analyze global spatial distributions, grid coverage, local-time sampling, and the effects of multi-mission joint observations. Bending angle, refractivity, and geometric height were further used to compare retrieval performance among missions.

ERA5 atmospheric reanalysis from the European Center for Medium-Range Weather Forecasts was used as the reference field for evaluating GNSS-RO retrieval products. ERA5 is the fifth-generation ECMWF global atmospheric reanalysis and provides continuous global estimates of atmospheric, land-surface, and oceanic variables (Hersbach et al., 2020). Globally gridded ERA5 data for 1 January 2026 were used at a horizontal resolution of 1° × 1° and a temporal resolution of 6 h (00:00, 06:00, 12:00, and 18:00 UTC). Temperature, pressure, and specific humidity were used to calculate reference refractivity profiles. These profiles were collocated with the bending angle, refractivity, and geometric-height information contained in the GNSS-RO BUFR data to calculate relative error, mean bias, and root-mean-square error.

https://doi.org/10.5194/egusphere-2026-4663
Preprint. Discussion started: 10 August 2026


## 3 Global distribution characteristics of individual missions

### 3.1 Coverage metrics and statistical methods

To quantify the global spatial coverage of each mission at a given spatial resolution, we introduce a grid-coverage metric. The global study area is first divided into $N_r$ grids at a prescribed latitude-longitude resolution r, and the number of RO events n_i(r) in the ith grid is counted. A grid is considered covered when it contains at least one RO event and is considered blank when it contains no events.

$$C(r) = \frac{\sum_{i=1}^{N_r} I(n_i(r) \geq 1)}{N_r x} \times 100\%,$$

$$I(n_i(r) \geq 1) = \begin{cases} 1, & n_{i(r)} \geq 1 \\ 0, & n_{i(r)} = 0 \end{cases} \quad (1)$$

In Eq. (1), C(r) is the global grid-coverage fraction at resolution r, N_r is the total number of grids included at that resolution, n_i(r) is the number of RO events in the ith grid, and I is the indicator function. The metric is the fraction of all grids containing RO observations and complements the blank-grid fraction (the fraction of grids without RO events), 1-C(r). Coverage was calculated at grid resolutions of 0.5, 1.0, and 2.0 degrees to compare global coverage continuity among individual missions and joint-observation scenarios.

To further characterize spatial gaps and observation concentration, we also use the blank-grid fraction and mean grid-event density. The blank-grid fraction describes the proportion of grids containing no RO events at a given spatial resolution and is defined as follows:

$$B(r) = 1 - C(r) \quad (2)$$

In Eq. (2), B(r) is the blank-grid fraction and C(r) is the grid-coverage fraction. This metric characterizes the spatial extent without RO observations.

In addition to coverage and blank-grid statistics, the average number of RO events within the gridded domain describes the overall observation concentration. The mean grid-event density is defined as follows:

$$D(r) = \frac{1}{N_r} \sum_{i=1}^{N_r} n_i(r) \quad (3)$$

In Eq. (3), D(r) is the mean grid-event density at resolution r and n_i(r) is the number of RO events in the ith grid.

### 3.2 Global spatial distributions

GNSS-RO events occur at the tangent points of signal paths between GNSS transmitters and receivers aboard low-Earth-orbit satellites. Figure 2 presents the global distributions of GNSS-RO events from COSMIC-2, FY-3, GRACE-C/D, KOMPSAT-5, MetOp-A/C, PAZ, PlanetiQ, Sentinel-6A, Spire, TerraSAR-X/TanDEM-X, TM-1, and YY-1 on 1 January 2026. During this one-day period, YY-1 produced the largest number of events (42,391), followed by TM-1 (34,506),

https://doi.org/10.5194/egusphere-2026-4663
Preprint. Discussion started: 10 August 2026


reflecting their comparatively large constellation sizes; the analysis included 33 YY-1 satellites and 22 TM-1 satellites. COSMIC-2 recorded the third-largest total (5,613), followed by PlanetiQ (4,658), Spire (4,523), and FY-3 (3,699). The low-inclination FY-3G satellite and YY-1 satellites 18–20 provided valuable supplementary observations at low latitudes, with FY-3G contributing 471 events and YY-1 satellites 18–20 contributing 1,826 events within 30°S–30°N. Owing to its near-circular low-inclination orbit configuration, COSMIC-2 provided dense and nearly symmetric tropical coverage, with 2,295 and 2,270 events occurring within 30°S–0° and 0°–30°N, respectively. PlanetiQ and Spire produced broad latitudinal coverage, with moderately enhanced sampling in the middle-latitude bands. MetOp-A/C and Sentinel-6A produced 1,153 and 1,007 events, respectively, whereas GRACE-C/D, TerraSAR-X/TanDEM-X, and PAZ produced 401, 238, and 140 events, resulting in less distinct spatial patterns. KOMPSAT-5 produced the fewest events (73), resulting in a distribution too sparse to support the identification of a robust spatial pattern. Localized data gaps apparent in some mission distributions, particularly over the Russia–Ukraine region, may be associated with regional signal interference, quality-control screening, or data-reception limitations; however, this interpretation remains tentative and requires independent verification.

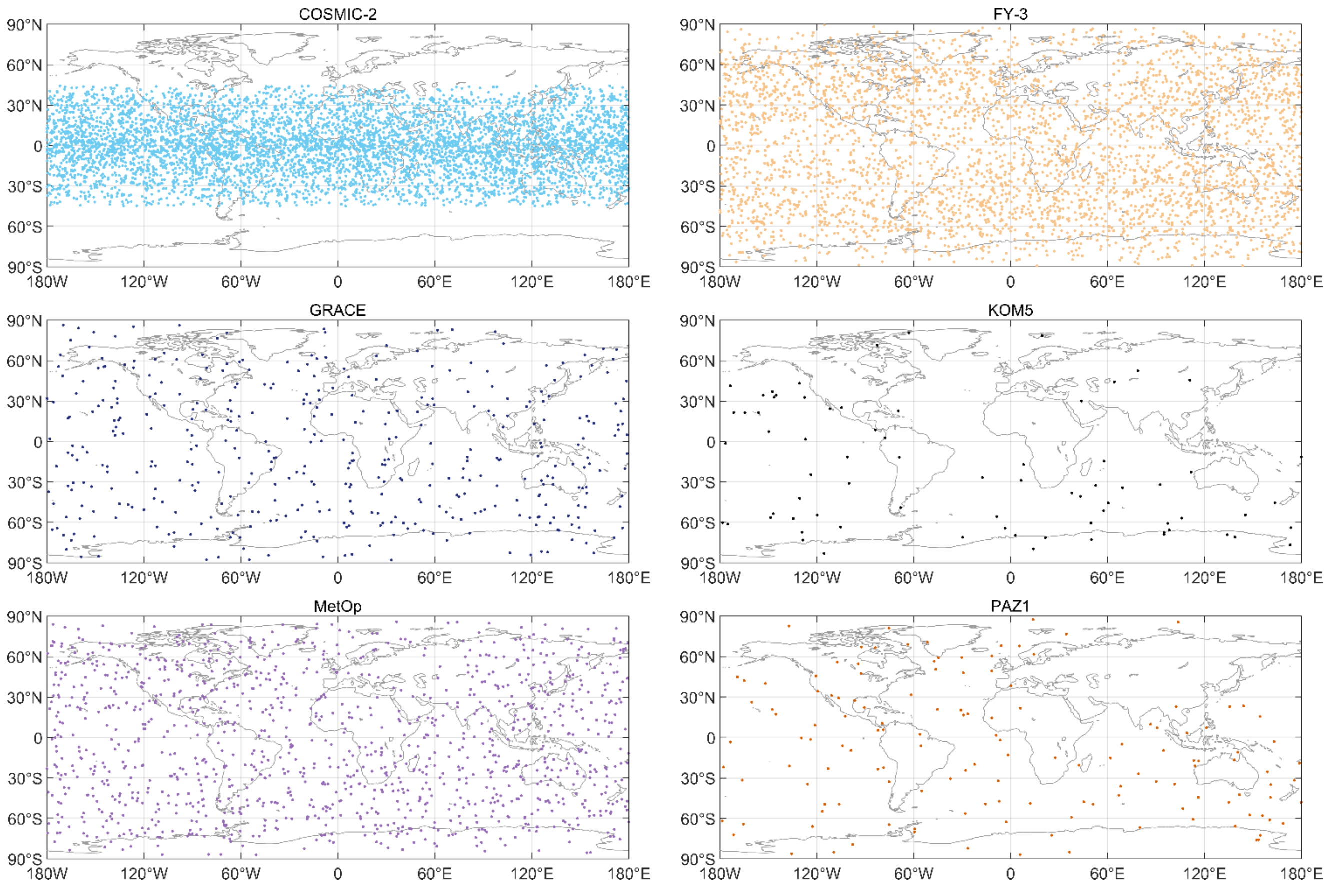

https://doi.org/10.5194/egusphere-2026-4663
Preprint. Discussion started: 10 August 2026


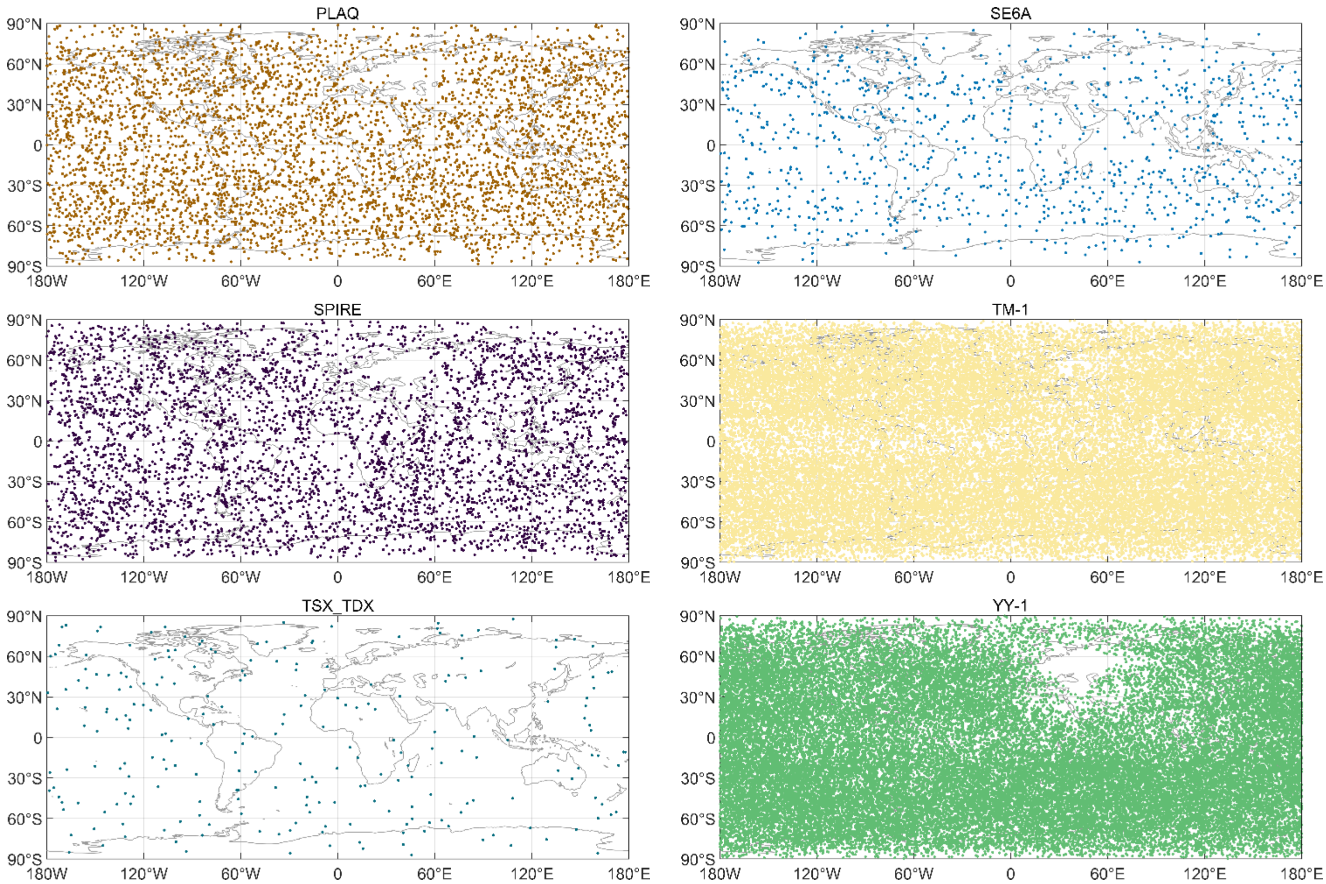


**Figure 2. Global distribution of radio occultation events from individual missions on 1 January 2026.**

### 3.3 Grid-based spatial distributions

Figure 3 presents gridded GNSS-RO event-density maps for 1–7 January 2026 at spatial resolutions of 0.5°, 1.0°, and 2.0°. For all missions, the fraction of zero-event grids decreases as grid size increases, and the seven-day accumulation substantially improves spatial continuity relative to the daily distribution. At 0.5° resolution, TM-1 and YY-1 already show much broader coverage than the other missions, with blank-grid fractions of 41.60% and 39.28%, respectively, whereas all other missions retain blank-grid fractions above 88%. At 1.0° resolution, TM-1 and YY-1 approach near-global continuity, with blank-grid fractions decreasing to 6.25% and 9.38%, respectively. At 2.0° resolution, TM-1 provides the most spatially continuous coverage, with only 0.69% blank grids and 16,089 nonzero grids, while YY-1 follows closely with 2.55% blank grids and 15,787 nonzero grids. YY-1, however, exhibits the strongest local event density, with a maximum of 64 events in a single 2.0° grid and 2,002 grids containing at least 30 events; the corresponding values for TM-1 are 42 events and 294 grids. The selected heatmap limits of 15, 40, and 70 events for the 0.5°, 1.0°, and 2.0° maps, respectively, remain above the observed maxima for all missions, so the color scaling preserves the full density range without saturation. Based on blank-grid fractions, nonzero-grid continuity, and maximum grid-level event density, the 12 systems can be broadly classified into

https://doi.org/10.5194/egusphere-2026-4663
Preprint. Discussion started: 10 August 2026


three tiers. The broad-coverage tier comprises TM-1 and YY-1, which provide the most extensive and continuous global sampling across all three resolutions. The intermediate tier includes PlanetiQ, Spire, FY-3, COSMIC-2, MetOp-A/C, and Sentinel-6A. Within this tier, PlanetiQ, Spire, and FY-3 show relatively strong 2.0° coverage, with blank-grid fractions of 19.53%, 20.81%, and 26.44%, respectively. COSMIC-2 shows a different pattern: its 2.0° blank-grid fraction is higher at 52.34%, but its sampling is concentrated within low latitudes, where the maximum number of events in a single 2.0° grid reaches 19. MetOp-A/C and Sentinel-6A remain less continuous, with 2.0° blank-grid fractions of 62.30% and 65.13%, respectively. The sparse tier comprises GRACE-C/D, TerraSAR-X/TanDEM-X, PAZ, and KOMPSAT-5. Their 2.0° blank-grid fractions remain high, at 84.11%, 87.72%, 92.51%, and 98.16%, respectively, indicating that their observations are still spatially discontinuous even after seven-day accumulation. Overall, the seven-day results show that TM-1 and YY-1 dominate the global event-density field, PlanetiQ, Spire, FY-3, and COSMIC-2 provide useful supplementary coverage with mission-specific spatial patterns, and the remaining smaller missions contribute more localized and sparse observations.

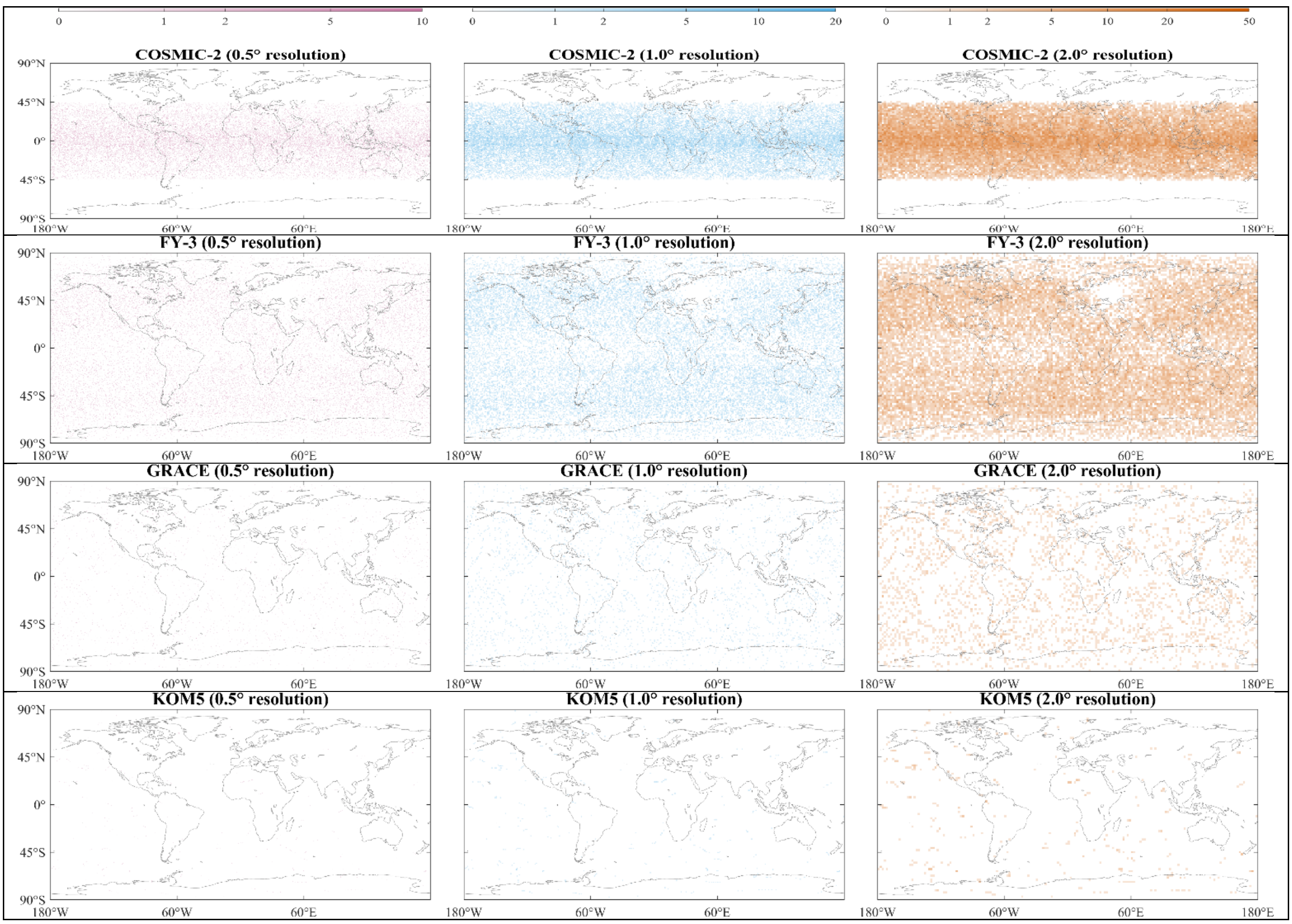

https://doi.org/10.5194/egusphere-2026-4663
Preprint. Discussion started: 10 August 2026


https://doi.org/10.5194/egusphere-2026-4663
Preprint. Discussion started: 10 August 2026


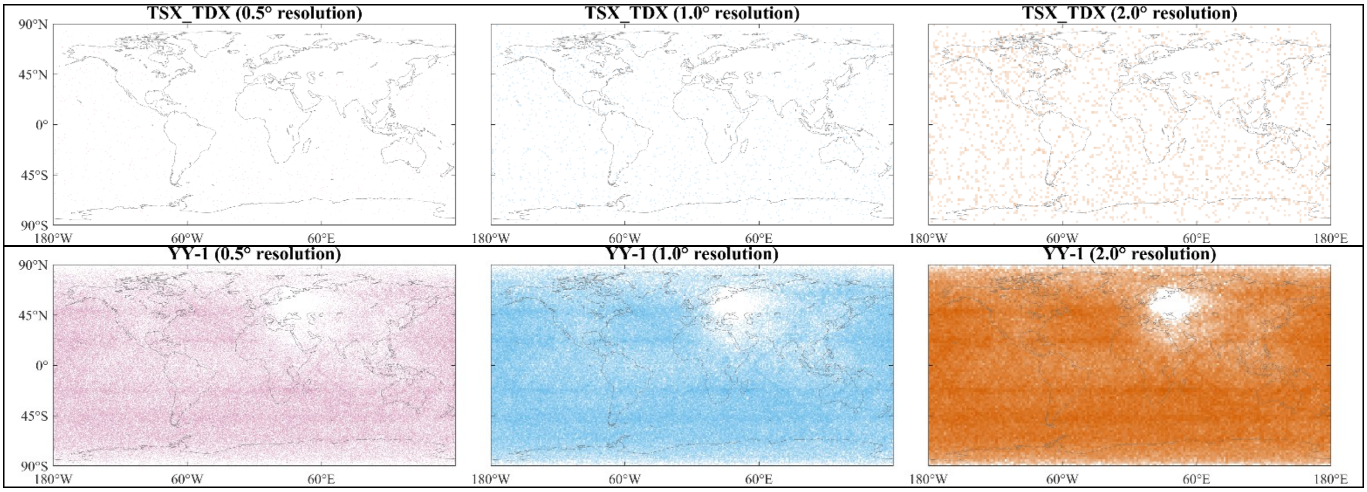


**Figure 3. Gridded spatial distributions of radio occultation events from individual missions during 1–7 January 2026.**

### 3.4 Local-time distributions

To analyze within-day temporal sampling, the UTC time of each event was converted to local time at the tangent point. Local time depends on both UTC and tangent-point longitude. Because the Earth rotates by approximately 15 degrees per hour, local time was calculated as follows:

$$LT = \left(UTC + \frac{\lambda}{15°}\right) mod\ 24 \quad (4)$$

In Eq. (4), LT is the local time of an RO event, UTC is the event time in coordinated universal time, and longitude is positive eastward and negative westward.

Figure 4 shows the local-time distributions of the global RO systems. The low-inclination COSMIC-2 configuration provides broad local-time sampling at low and middle latitudes. The local-time distributions of FY-3D, FY-3E, and FY-3F correspond to their descending-node local times, while low-inclination FY-3G produces curved bands that supplement low-latitude sampling. Sentinel-6A exhibits a similar curved-band pattern. The near-polar GRACE-C/D configuration produces nearly meridional distributions near 01:30, 11:30, 13:30, and 23:30 local time. Too few KOMPSAT-5 events are available to identify a clear pattern. MetOp-A/C events cluster near 08:00-10:00 and 20:00-22:00, while TerraSAR-X/TanDEM-X and PAZ events cluster near 05:00-07:00 and 17:00-19:00, consistent with their approximately 06:00 descending-node local times. Spire events primarily occur near 10:00-12:00 and 22:00-24:00. PlanetiQ has many events concentrated near 08:00-12:00 and 20:00-24:00, although the cause of this pattern requires further investigation. TM-1 includes sun-synchronous satellites with different descending-node local times, providing observations throughout the day but retaining gaps associated with LEO-GNSS geometry. Many YY-1 sun-synchronous satellites have descending-node local times between

https://doi.org/10.5194/egusphere-2026-4663
Preprint. Discussion started: 10 August 2026


02:00 and 08:00, producing concentrated sampling, while YY-1 satellites 18-20 supplement low-latitude gaps. Overall, mission-specific orbital objectives and local-time configurations produce pronounced sampling biases, particularly because many near-sun-synchronous satellites are concentrated near 08:00-12:00 local time.

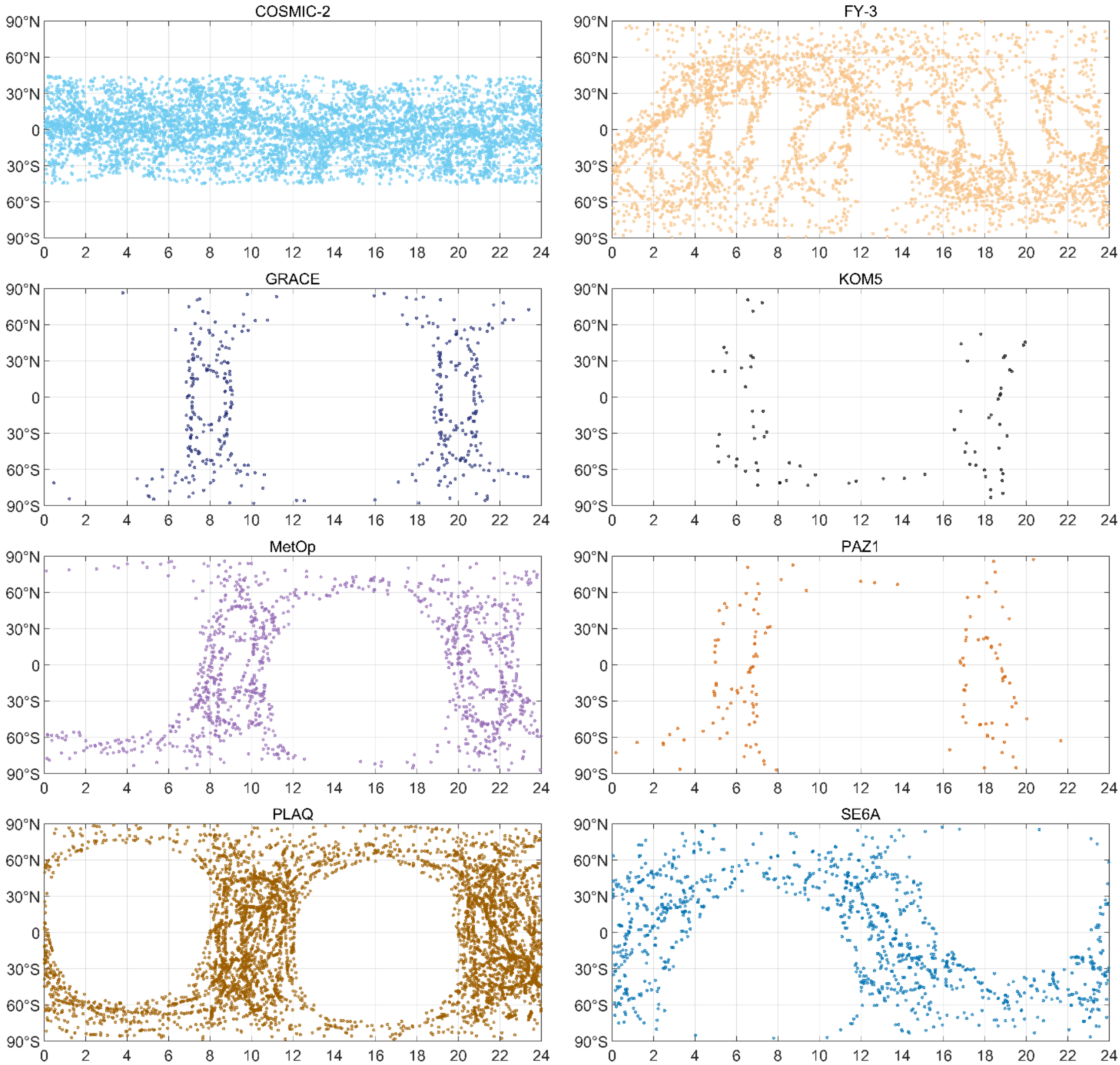

https://doi.org/10.5194/egusphere-2026-4663
Preprint. Discussion started: 10 August 2026


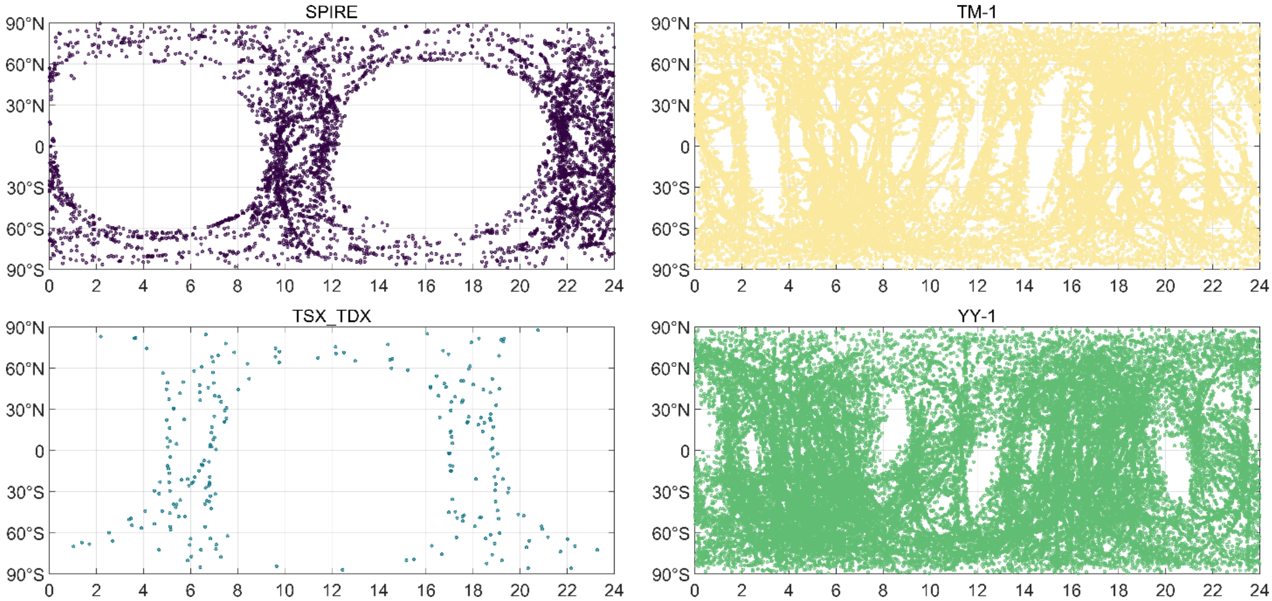


**Figure 4. Local-time distributions of radio occultation events from individual missions on 1 January 2026.**

### 3.5 Coverage within 6 h time windows

To assess coverage on the time scale commonly used for numerical weather prediction data assimilation, RO events on 1 January 2026 were divided into four 6 h UTC windows: 00:00–06:00, 06:00–12:00, 12:00–18:00, and 18:00–24:00. Global grid coverage was calculated for each window at spatial resolutions of 0.5°, 1.0°, and 2.0°. Compared with daily statistics, 6 h coverage more directly characterizes short-term spatial continuity within a typical assimilation window. The results are shown in Fig. 5. For this one-day sample, mission-averaged coverage was broadly similar among the four UTC windows, although the temporal variability differed among missions. At 2.0° resolution, the mean coverage across all missions was 8.88%, 9.71%, 9.29%, and 9.15% in the four successive windows, with corresponding total event counts of 23,462, 25,911, 24,442, and 24,587. YY-1 and TM-1 retained the strongest global coverage at the 6 h scale. The mean YY-1 coverage fractions at 0.5°, 1.0°, and 2.0° were 3.85%, 14.06%, and 41.88%, respectively, compared with 3.25%, 12.12%, and 38.24% for TM-1. YY-1 reached the highest 2.0° coverage in the 06:00–12:00 UTC window (45.87%), whereas TM-1 remained more temporally stable, with 2.0° coverage ranging only from 37.40% to 39.35%. Thus, even within 6 h windows, large constellations maintained high global grid coverage and were the principal contributors to short-term global observational continuity. COSMIC-2, PlanetiQ, Spire, and FY-3 provided moderate 6 h coverage. Their mean coverage fractions at 0.5°, 1.0°, and 2.0° were 0.54%, 2.11%, and 7.83% for COSMIC-2; 0.45%, 1.78%, and 6.80% for PlanetiQ; 0.43%, 1.70%, and 6.33% for Spire; and 0.35%, 1.40%, and 5.44% for FY-3. COSMIC-2 coverage increased from 6.82% in the first window to more than 8.4% in the last two windows at 2.0° resolution, whereas FY-3 was comparatively stable, with 2.0° coverage ranging from 5.05% to 5.59%. Spire showed stronger window dependence, with 2.0° coverage decreasing from 7.83% in the first window to 4.43% in the final window. Although these missions provided less coverage than YY-1 and TM-1, they still

https://doi.org/10.5194/egusphere-2026-4663
Preprint. Discussion started: 10 August 2026


supplied important complementary observations within 6 h assimilation windows. Single-satellite and small-constellation missions generally provided low coverage within 6 h windows. At 2.0° resolution, the mean coverage fractions for GRACE-C/D, KOMPSAT-5, PAZ, and TerraSAR-X/TanDEM-X were 0.62%, 0.11%, 0.22%, and 0.37%, respectively. MetOp-A/C and Sentinel-6A achieved slightly higher mean coverage, but only 1.75% and 1.54%, respectively. These missions may provide useful spatial samples on a daily scale, but they still leave pronounced global gaps when used alone within a 6 h data-assimilation window. Overall, the results indicate that 6 h coverage was governed primarily by event abundance and constellation size, while orbital configuration affected how efficiently those events translated into spatial coverage. Across the analyzed windows and resolutions, the Pearson correlation between mission event count and coverage ranged from 0.996 to 1.000. Large constellations therefore had a clear advantage at the 6 h scale, whereas individual satellites and small constellations provided limited stand-alone coverage. Because the analysis was based on only four windows from a single day, these findings should be interpreted as descriptive evidence for 1 January 2026 rather than as proof of general independence from the UTC window. Multi-mission observations remain essential for improving global continuity and reducing spatial gaps in short-window applications such as numerical weather prediction data assimilation.

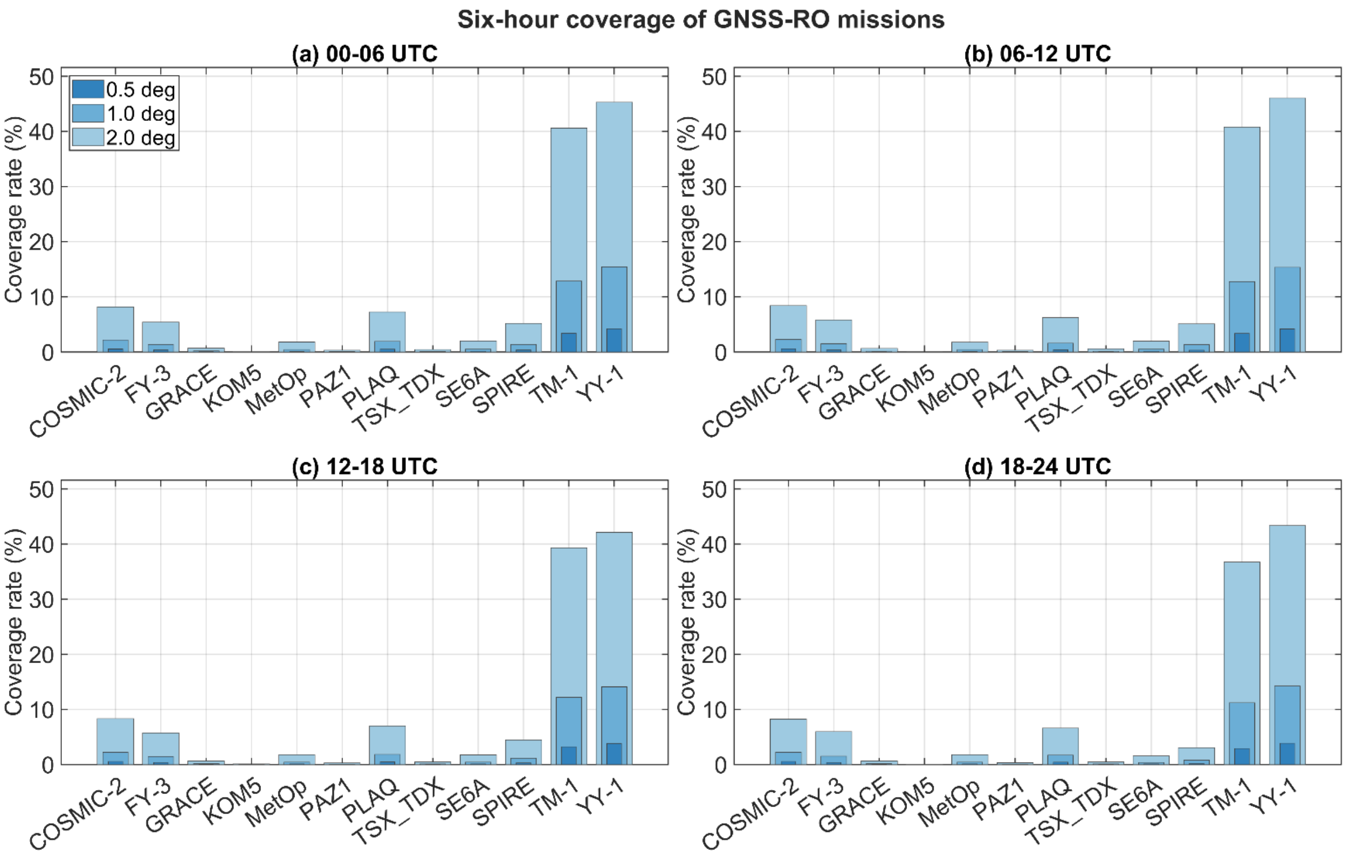


**Figure 5. Coverage of individual GNSS-RO missions within 6 h time windows on 1 January 2026.**

https://doi.org/10.5194/egusphere-2026-4663
Preprint. Discussion started: 10 August 2026


## 4 Joint distribution characteristics of global GNSS-RO missions

Observations from all missions analyzed in Sect. 3 were combined to evaluate the overall effects of multi-mission joint observations.

$$n_i^{joint}(r) = \sum_{k=1}^{M} n_{(i,k)}(r) \quad (5)$$

In Eq. (5), n_i, joint(r) is the total number of RO events in the ith grid after combining missions at spatial resolution r, n_i, m(r) is the number of events from mission m in the ith grid, and M is the number of missions included in the joint analysis.

### 4.1 Joint global spatial distribution

Figure 6 shows the enhanced spatial completeness achieved by combining observations from all missions on 1 January 2026. The joint dataset contains 98,402 GNSS-RO events and provides substantially broader global sampling than any individual mission. The complementarity is particularly evident at low latitudes and in polar regions. At low latitudes, observations from the low-inclination FY-3G satellite and YY-1 satellites 18–20 complement the dense tropical sampling of COSMIC-2. Within 10° of the Equator, the combined dataset contains 10,979 events, accounting for 11.16% of the joint sample. Within 30°S–30°N, COSMIC-2 contributes 4,565 events, while FY-3G and YY-1 satellites 18–20 contribute 471 and 1,826 events, respectively, thereby strengthening the low-latitude observing capability. Polar sampling is also enhanced through the complementarity of high-inclination and near-polar missions. A total of 21,762 events occur poleward of 60°, accounting for 22.12% of the joint sample, with YY-1, TM-1, PlanetiQ, Spire, FY-3, and other high-inclination missions jointly contributing to high-latitude coverage. Overall, the combined dataset demonstrates clear latitudinal complementarity among missions: COSMIC-2 and selected low-inclination satellites strengthen tropical coverage, whereas high-inclination and near-polar missions improve sampling in polar regions. Localized data gaps near the Russia–Ukraine region are still visible in some distributions and may be related to regional signal interference, quality-control screening, or data-reception limitations.

https://doi.org/10.5194/egusphere-2026-4663
Preprint. Discussion started: 10 August 2026


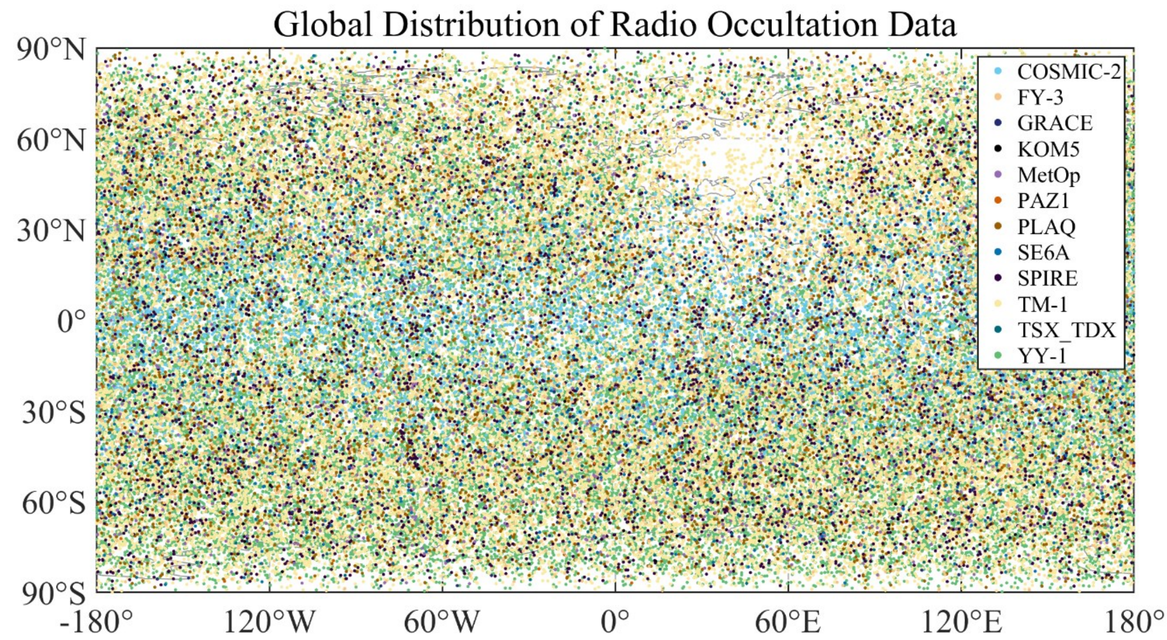


**Figure 6. Global distribution of the combined radio occultation dataset on 1 January 2026.**

### 4.2 Joint global gridded distribution

Figure 7 further illustrates the event density and spatial continuity achieved by combining 679,854 RO events from all missions during 1–7 January 2026. At 0.5° resolution, 225,142 of the 259,200 global grids are occupied, corresponding to a spatial coverage of 86.86% and a blank-grid fraction of 13.14%; the maximum density reaches 15 events per grid. Most occupied grids remain low to moderate in density, with 102,993 grids containing one to two events and 79,607 grids containing three to four events, whereas only 681 grids contain ten or more events. At 1.0° resolution, the blank-grid fraction decreases to 1.87%, and the maximum density increases to 38 events per grid. The largest density class is 10–14 events, comprising 22,559 grids, while 34 grids contain 30 or more events. At 2.0° resolution, the combined dataset provides nearly continuous global coverage, with 16,170 of 16,200 grids occupied, a blank-grid fraction of only 0.19%, and a maximum density of 113 events per grid. The dominant density class is 40–59 events, accounting for 7,205 grids, followed by 60–79 events in 2,294 grids; only three grids contain 100 or more events. The heat-map distribution also exhibits clear zonal high-density bands. Pronounced dense regions appear near approximately 20°S and 20°N, while another relatively evident concentration occurs around 45° latitude in both hemispheres. These banded structures indicate that, although multi-mission combination greatly improves global spatial continuity, the final event-density pattern still reflects the combined influence of orbital inclination, constellation geometry, and latitude-dependent sampling frequency.

https://doi.org/10.5194/egusphere-2026-4663
Preprint. Discussion started: 10 August 2026


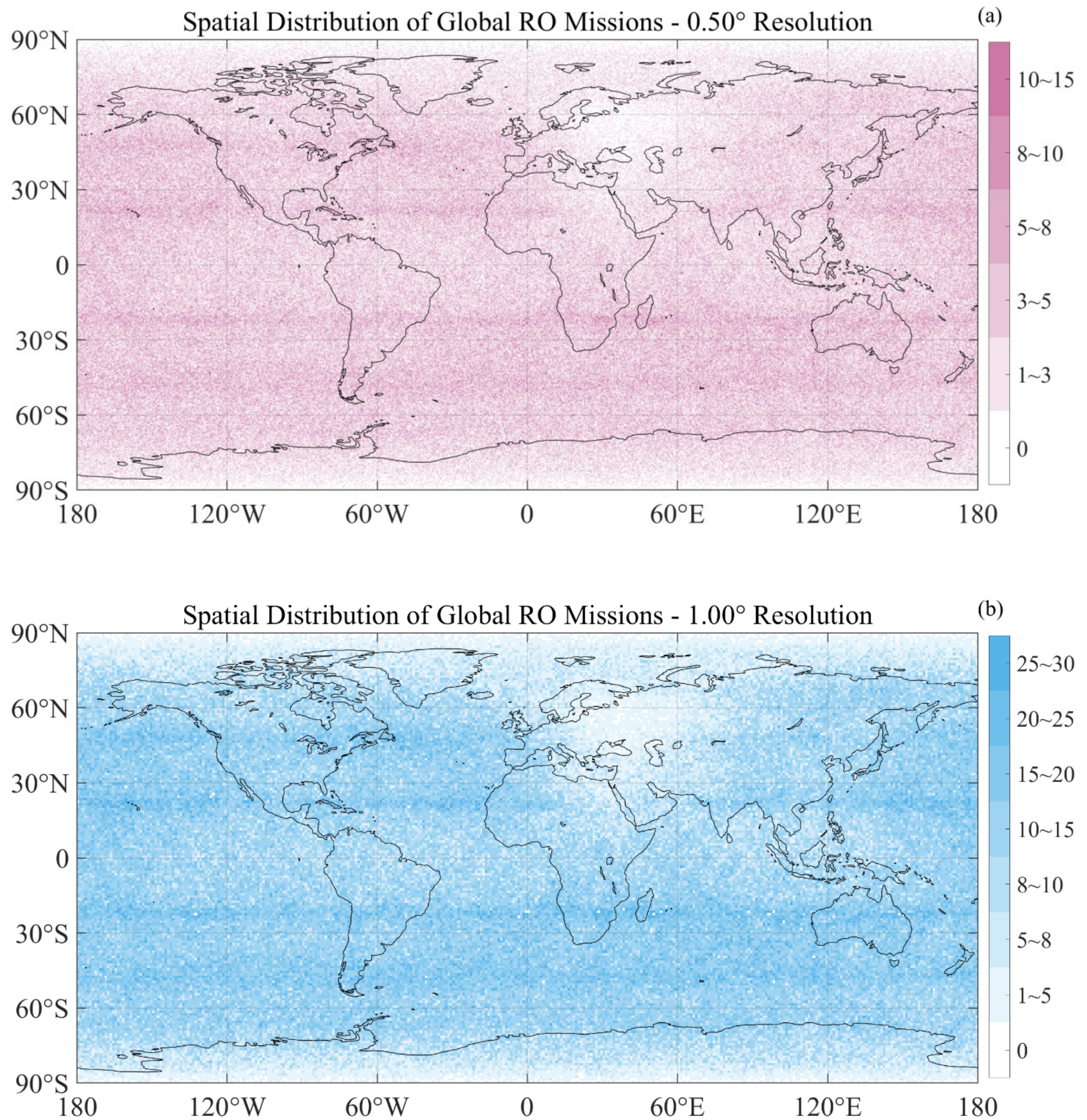

https://doi.org/10.5194/egusphere-2026-4663
Preprint. Discussion started: 10 August 2026


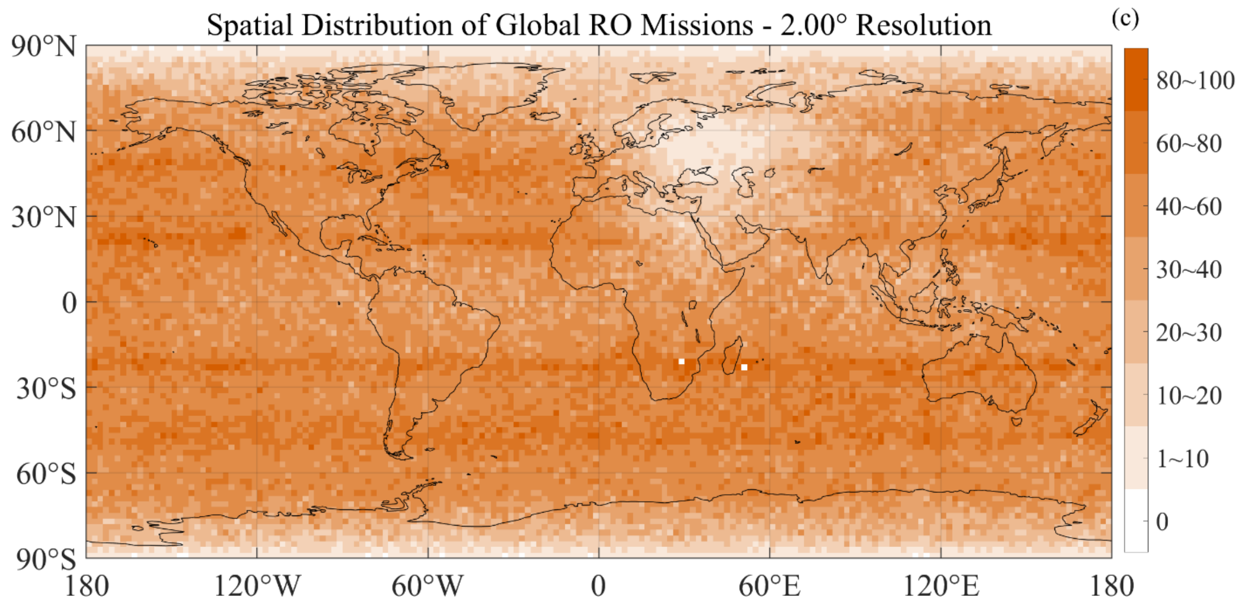


**Figure 7. Gridded spatial distribution of the combined radio occultation dataset during 1–7 January 2026.**

### 4.3 Joint global local-time distribution

Figure 8 shows that combining observations from multiple missions broadens and densifies the latitude–local-time distribution and reduces mission-specific sampling gaps on 1 January 2026. The joint dataset contains 98,402 RO events, of which YY-1 and TM-1 jointly contribute 76,897 events, accounting for 78.15% of the total. Owing to their large constellation sizes and relatively distributed local-time sampling geometry, YY-1 and TM-1 provide the main observational backbone for the combined dataset and substantially enhance global latitude–local-time continuity. FY-3 also contributes to a more balanced local-time distribution: the differing local-time designs of FY-3D, FY-3E, and FY-3F help spread observations across multiple time sectors, while the low-inclination FY-3G satellite provides additional sampling at low latitudes. COSMIC-2 and YY-1 satellites 18–20 further strengthen the low-latitude component of the combined distribution. Other missions exhibit more distinct mission-dependent local-time preferences. For example, near-polar or sun-synchronous missions such as PlanetiQ, Spire, MetOp, GRACE-C/D, KOMPSAT-5, PAZ, and TerraSAR-X/TanDEM-X tend to form localized or banded structures in specific morning, evening, or nighttime local-time sectors, rather than providing uniformly distributed sampling on their own. Overall, the multi-mission combination produces a more continuous local-time distribution than any single constellation or mission alone. Nevertheless, the sampling remains nonuniform, with event density varying among latitude bands and local-time sectors, reflecting the combined effects of constellation size, orbital configuration, and mission-specific sampling geometry.

https://doi.org/10.5194/egusphere-2026-4663
Preprint. Discussion started: 10 August 2026


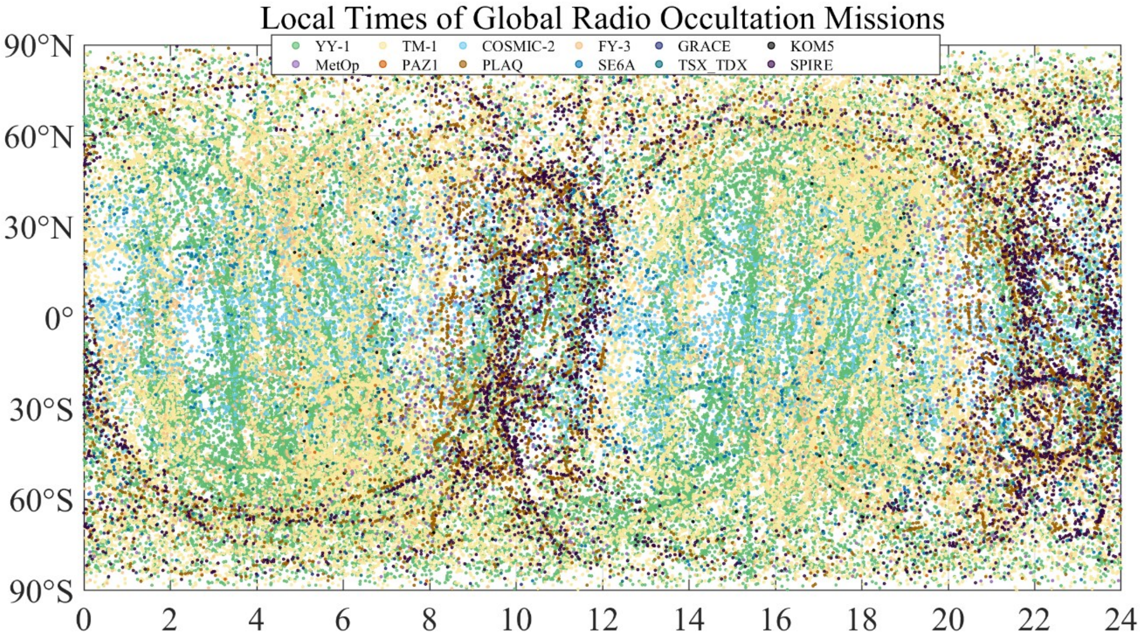


Figure 8. Local-time distribution of the combined radio occultation dataset **on 1 January 2026**.

### 4.4 Joint coverage within 6 h time windows

To assess joint coverage on the time scale commonly used for numerical weather prediction data assimilation, the multi-mission analysis employed the same four 6 h UTC windows used in the individual-mission analysis. This consistent temporal framework enables direct comparison between individual and combined RO observations within operationally relevant assimilation windows.

**Table 2. Mean 6 h global grid coverage (%) of individual RO missions and the combined dataset at three spatial resolutions**

| Mission | 0.5° | 1.0° | 2.0° |
|---|---|---|---|
| Combined dataset | 8.831 | 29.944 | 70.978 |
| COSMIC-2 | 0.538 | 2.108 | 7.833 |
| FY-3 | 0.354 | 1.404 | 5.435 |
| GRACE-C/D | 0.039 | 0.155 | 0.619 |
| KOMPSAT-5 | 0.007 | 0.028 | 0.113 |
| MetOp | 0.111 | 0.443 | 1.752 |
| PAZ | 0.014 | 0.054 | 0.216 |
| PlanetiQ | 0.448 | 1.776 | 6.802 |
| TerraSAR- | 0.023 | 0.092 | 0.367 |

https://doi.org/10.5194/egusphere-2026-4663
Preprint. Discussion started: 10 August 2026


| | | | |
|---|---|---|---|
| X/TanDEM-X | | | |
| Sentinel-6A | 0.097 | 0.387 | 1.535 |
| Spire | 0.434 | 1.703 | 6.326 |
| TM-1 | 3.247 | 12.121 | 38.236 |
| YY-1 | 3.848 | 14.056 | 41.883 |

To quantify the improvement in 6 h coverage achieved through multi-mission integration, the combined dataset was compared with the individual RO missions. Coverage was calculated separately for each spatial resolution and 6 h window on 1 January 2026 and then averaged across the four windows.

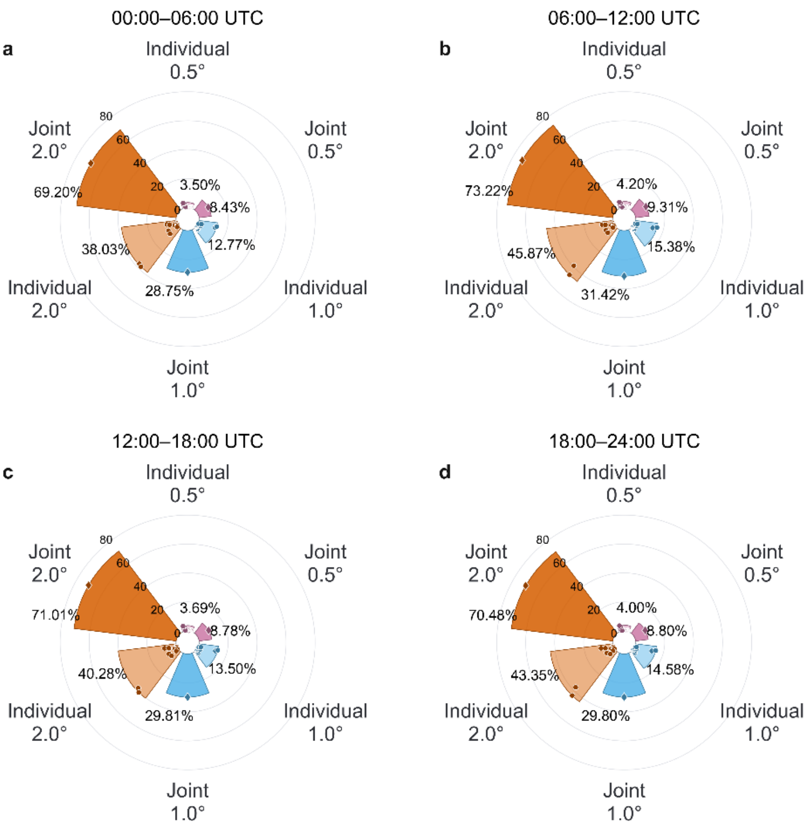


**Figure 9. Global coverage in four 6 h UTC windows on 1 January 2026**

Figure 9 presents the results for individual windows, whereas Table 2 reports their four-window means. Averaged over the four windows, joint coverage reaches 8.83, 29.94, and 70.98% at 0.5°, 1.0°, and 2.0°, respectively. YY-1 remains the best-performing individual mission, with corresponding mean coverage fractions of 3.85, 14.06, and 41.88%. Joint observations therefore provide absolute gains of 4.98, 15.89, and 29.10 percentage points relative to YY-1, equivalent to relative increases of 129.5, 113.0, and 69.5%. Although the proportional improvement decreases as grid size increases, the absolute coverage

https://doi.org/10.5194/egusphere-2026-4663
Preprint. Discussion started: 10 August 2026


gain becomes larger. These results demonstrate that complementary sampling among missions effectively fills additional spatial gaps and improves global observational continuity within 6 h data-assimilation windows.

### 4.5 Potential impact of COSMIC-2 retirement on joint GNSS-RO coverage

To assess the potential impact of the planned retirement of COSMIC-2, the joint GNSS-RO dataset was re-evaluated after excluding COSMIC-2 and retaining the other 11 missions. Figure 10 compares the latitudinal distributions of the 11-mission dataset, the complete 12-mission dataset, and COSMIC-2 alone. The removal of COSMIC-2 has a distinctly latitude-dependent effect. Because COSMIC-2 is a low-inclination constellation, its contribution is concentrated in the tropical and subtropical regions, whereas the remaining missions largely preserve the mid- and high-latitude sampling structure. Within 5°S–5°N, the number of RO events decreases from 5,539 for the 12-mission dataset to 4,334 after removal of COSMIC-2, corresponding to a reduction of 1,205 events (21.75%). Thus, although the remaining 11 missions still provide extensive global sampling, the retirement of COSMIC-2 would noticeably weaken the latitudinal sampling density near the Equator.

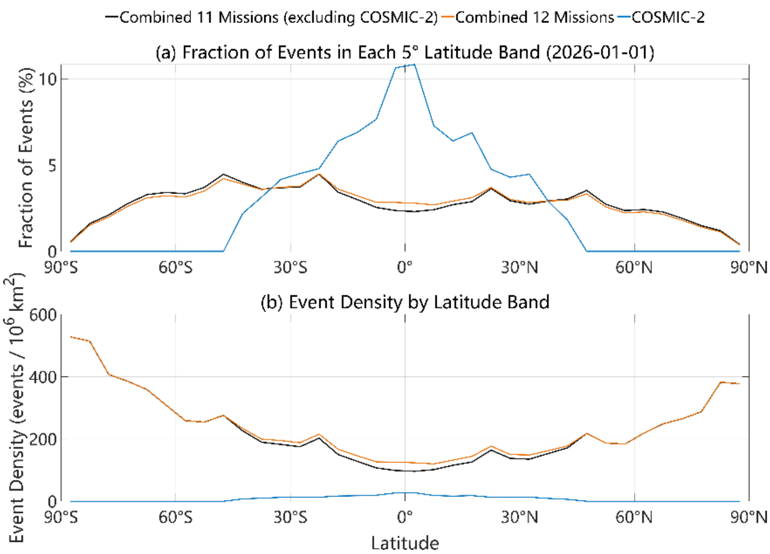


**Figure 10. Latitudinal distributions of GNSS-RO events for the combined 11-mission dataset excluding COSMIC-2, the complete 12-mission dataset, and COSMIC-2 alone on 1 January 2026.**

Figure 11 further illustrates the spatially irreplaceable contribution of COSMIC-2 at three grid resolutions: (a) 0.5° × 0.5°, (b) 1° × 1°, and (c) 2° × 2°. Gray grids are covered by the other 11 missions, red grids are covered only by COSMIC-2, and white grids are not covered by any of the 12 missions. At the finest 0.5° resolution, 3,797 grids, corresponding to 2.16% of the global area, are covered exclusively by COSMIC-2. These COSMIC-2-only grids are concentrated in the low- and middle-latitude belt, with a pronounced tropical contribution, confirming that the constellation provides coverage that cannot be fully replaced by the other missions at high spatial resolution. At 1° resolution, the COSMIC-2-only coverage fraction is 2.82% (1,233 grids), whereas at 2° resolution it decreases to 0.28% (31 grids) because the coarser grid aggregation merges many COSMIC-2 observations with coverage from the other missions. Overall, the multi-mission system remains highly

https://doi.org/10.5194/egusphere-2026-4663
Preprint. Discussion started: 10 August 2026


resilient after excluding COSMIC-2, especially at coarse spatial scales; however, its retirement would lead to a measurable loss of independent high-resolution coverage and a clear reduction in equatorial RO sampling.

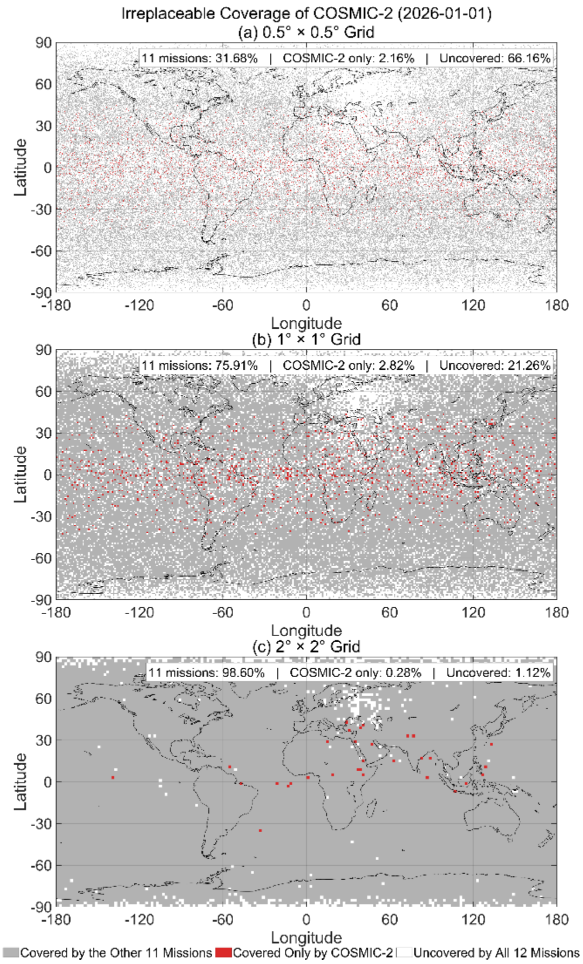


**Figure 11. Spatially irreplaceable coverage contribution of COSMIC-2 at 0.5°, 1°, and 2° grid resolutions on 1 January 2026.**

## 5 Comparison of GNSS-RO retrievals with ERA5

### 5.1 Method for comparison with ERA5

ERA5 reference neutral-atmospheric refractivity was calculated from pressure, temperature, and specific humidity using the Smith–Weintraub equation (Smith and Weintraub, 1953):

$$N = 77.6\frac{p}{T} + 3.73 \times 10^{5}\frac{e}{T^{2}} \quad (6)$$

https://doi.org/10.5194/egusphere-2026-4663
Preprint. Discussion started: 10 August 2026


where N is the neutral-atmospheric refractivity in N-units, \(p\) is the total atmospheric pressure in hPa, \(T\) is the absolute temperature in K, and \(e\) is the water-vapor partial pressure in hPa. Water-vapor pressure was calculated from ERA5 specific humidity q as follows:

$$e = \frac{qp}{0.622 + 0.378q} \tag{7}$$

After calculating ERA5 reference refractivity profiles, the forward-modeling method implemented in the Radio Occultation Processing Package (ROPP) was followed. The profiles were vertically interpolated at high resolution, and the corresponding impact parameters and refractive-index gradients were calculated. ERA5 reference bending angles were then obtained using an Abel integral and compared with RO Level 1b bending-angle products. First, the ERA5 refractivity profiles were logarithmically interpolated in the vertical, and refractive index was calculated as follows:

$$n(r) = 1 + N(r) \times 10^{-6} \tag{8}$$

In Eq. (7), n(r) is refractive index, N(r) is atmospheric refractivity, and r is the radial distance from the center of the Earth. The corresponding impact parameter is defined as follows:

$$a = n(r)r \tag{9}$$

Under the assumption of spherical symmetry, bending angle is calculated from the radial gradient of refractive index using the Abel integral (Fjeldbo et al., 1971):

$$\alpha(a) = -2a \int_{r_a}^{\infty} \frac{d \ln n(r)}{dr} \frac{dr}{\sqrt{n^2(r)r^2 - a^2}} \tag{10}$$

In Eq. (10), alpha(a) is the bending angle associated with impact parameter a, and r_t is the corresponding tangent-point radius.

Relative error and root mean square error (RMSE) were used to quantify bending-angle and refractivity retrieval errors. Relative error is defined as follows:

$$\delta X(z) = \frac{X_{RO(z)} - X_{ERA5(z)}}{X_{ERA5(z)}} \times 100\% \tag{11}$$

In Eq. (11), x represents bending angle or refractivity and z is geometric height.

To characterize systematic differences between each mission and the ERA5 reference, the mean bias was calculated at each geometric-height level as follows:

$$Bias(z) = \frac{1}{N_z} \sum_{i=1}^{N_z} [\delta X_i(z)] \tag{12}$$

The overall error magnitude was additionally evaluated using RMSE:

https://doi.org/10.5194/egusphere-2026-4663
Preprint. Discussion started: 10 August 2026


$$RMSE(z) = \sqrt{\frac{1}{N_z}\sum_{i=1}^{N_z}[\delta X_i(z)]^2} \qquad (13)$$

In Eq. (13), $N_z$ is the number of samples included at height z.

### 5.2 ERA5-based bending-angle and refractivity error analysis

Following the method described in Sect. 5.1, vertical profiles of bending-angle and refractivity errors relative to ERA5 were calculated for each mission (Fig. 12a).

Bending-angle errors propagate into the subsequent Abel inversion and are particularly sensitive to receiver tracking quality, orbit and clock corrections, residual ionospheric correction, and horizontal gradients in the lower atmosphere. Figure 12a shows distinct vertical error structures among the missions. Above approximately 47 km, all missions exhibit negative biases of varying magnitude. This common high-altitude tendency may arise because neutral-atmospheric bending becomes very small with increasing altitude, making relative-error statistics increasingly sensitive to measurement noise, residual ionospheric effects, and orbit and clock correction errors. COSMIC-2 exhibits a pronounced positive bias in the middle atmosphere, with the most prominent feature occurring near 20 km. Its RMSE between 10 and 30 km is substantially larger than that of the other missions. Below 10 km, the RMSE increases progressively toward the surface and remains considerably larger than that of the other missions. These features may be related to the low-inclination orbit and predominantly tropical sampling of COSMIC-2. Strong horizontal inhomogeneity, high water-vapor content, and steep vertical moisture gradients in the tropics increase the likelihood of super-refraction, multipath propagation, and unstable signal tracking. Sentinel-6A reaches its maximum positive bias at approximately 3–4 km. GRACE-C/D maintains a positive bias throughout the lower atmosphere. The pronounced bending-angle error of Sentinel-6A at the lowest level may be attributed to the limited number of valid profiles, resulting in considerable statistical uncertainty. Owing to their relatively small sample sizes, the bending-angle error profiles of KOMPSAT-5, PAZ and TerraSAR-X/TanDEM-X are less smooth and subject to greater statistical uncertainty. For most other missions, mean biases in the middle and upper atmosphere remain close to zero, and RMSE varies relatively smoothly with height. In the lower troposphere, the missions exhibit negative biases of varying magnitudes because of strong moisture gradients, super-refraction, multipath propagation, and other complexities in the near-surface propagation environment.

Figure 12b shows the refractivity retrieval errors for the same period. Between 5 and 35 km, mean refractivity biases are generally below 1% and centered near zero, indicating stable retrievals for most missions. COSMIC-2 exhibits a small positive bias between 10 and 30 km, consistent with its bending-angle error characteristics. Apart from COSMIC-2, the retrieval accuracy of the different missions is broadly consistent between 10 and 35 km. Inter-mission differences become more pronounced in the lower troposphere, particularly below 5 km. PAZ develops a negative bias at a higher altitude than the other missions, possibly because its dual-polarization RO mode tracks only setting occultations. Below 10 km,

https://doi.org/10.5194/egusphere-2026-4663
Preprint. Discussion started: 10 August 2026


TerraSAR-X/TanDEM-X exhibits a vertical error structure distinct from those of the other missions: a negative bias first appears at approximately 3–5 km, followed by a positive bias near 2.5 km, which subsequently shifts back to a negative bias toward the surface. Most other missions show a positive bias followed by a negative bias toward the surface, reflecting the combined effects of complex near-surface moisture structures, multipath propagation, and signal truncation. GRACE-C/D shows a small positive bias at the lowest level, although the underlying cause remains unclear. Above 35 km, all missions exhibit a broadly consistent vertical variation in refractivity bias, while COSMIC-2 has the largest overall bias magnitude. This common upper-level behavior may reflect the propagation of bending-angle biases into the refractivity retrievals, as well as errors associated with upper-level reference fields or retrieval initialization. Differences in sampling and atmospheric representativeness among orbital configurations may further modulate the magnitude of these biases.

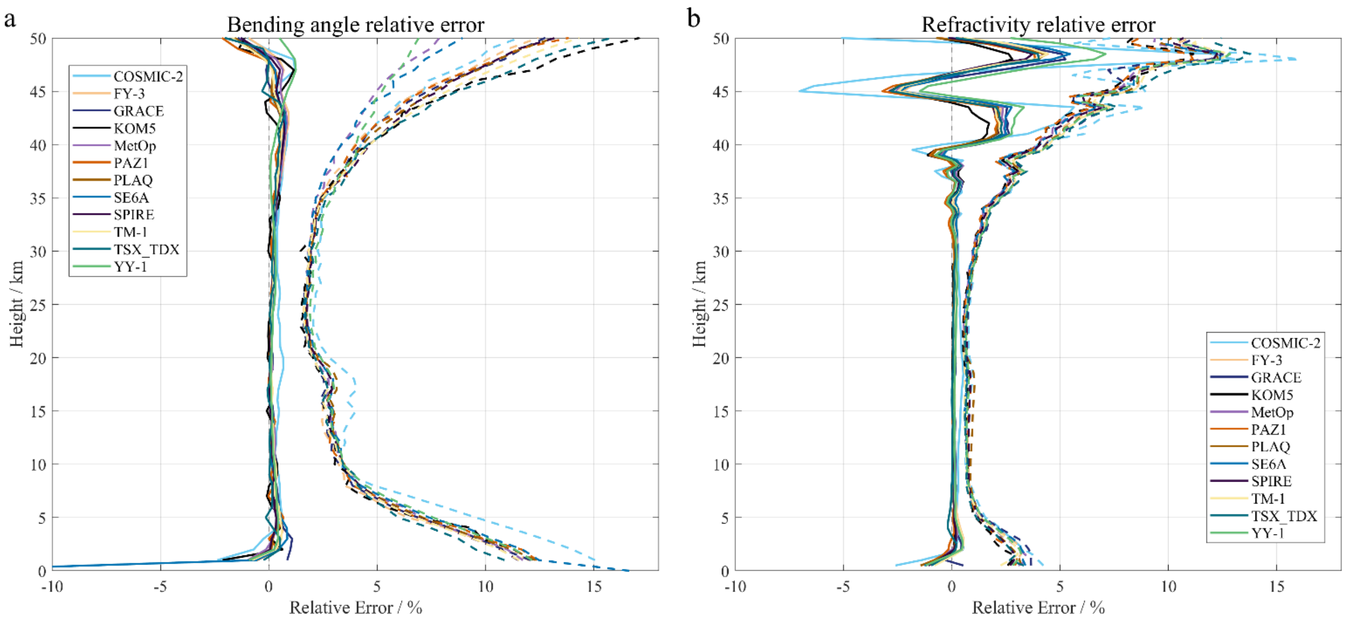


**Figure 12. Vertical profiles of mean relative bias (solid lines) and relative root mean square error (dashed lines) for (a) bending angle and (b) refractivity from individual GNSS-RO missions relative to ERA5.**

## 6 Conclusions and outlook

This study compared the spatial distributions, grid coverage, local-time sampling, 6 h coverage, and retrieval characteristics of 12 GNSS-RO mission systems using observations collected during 1–7 January 2026. The results demonstrate that constellation size, event abundance, and orbital configuration jointly determine the observational capabilities of individual missions. Large constellations provide the strongest global spatial continuity, low-inclination missions enhance tropical and subtropical sampling, and high-inclination and near-polar missions provide complementary observations at middle and high latitudes. Consequently, no single mission can reproduce the spatial and temporal sampling characteristics of the complete multi-mission observing system.

https://doi.org/10.5194/egusphere-2026-4663
Preprint. Discussion started: 10 August 2026


On 1 January 2026, the combined dataset contained 98,402 RO events, of which YY-1 and TM-1 contributed 78.15%. Their large observation volumes formed the backbone of the global distribution, while COSMIC-2, FY-3G, and the low-inclination YY-1 satellites strengthened tropical sampling. Over the full seven-day period, the combined dataset comprised 679,854 events. Its global grid coverage reached 86.86%, 98.13%, and 99.81% at resolutions of 0.5°, 1.0°, and 2.0°, respectively. Although the integrated dataset provided nearly continuous global coverage at the two coarser resolutions, its event density remained spatially nonuniform, with pronounced zonal structures associated with orbital inclination, constellation geometry, and latitude-dependent sampling frequency.

At the 6 h scale relevant to numerical weather prediction data assimilation, event abundance was strongly correlated with grid coverage. Multi-mission integration substantially improved short-window spatial continuity, achieving 70.98% coverage at 2.0° resolution compared with 41.88% for YY-1, the best-performing individual mission. The combined observations also broadened sampling across the 24 h local-time cycle and reduced gaps among latitude bands, demonstrating the benefits of complementary orbital configurations.

Comparisons with ERA5 indicate that both bending-angle and refractivity retrievals from most missions show broadly consistent performance in the middle and upper atmosphere. For bending angle, mean relative biases for most missions remain close to zero at middle and upper levels, although a common negative tendency appears above approximately 47 km, where the weak neutral-atmospheric signal increases the sensitivity of relative errors to measurement noise and residual retrieval errors. COSMIC-2 exhibits a pronounced positive bias near 20 km and larger RMSE values between 10 and 30 km, while its errors increase markedly toward the surface. These features are likely associated with its predominantly tropical sampling, where strong moisture gradients, super-refraction, multipath propagation, and unstable tracking conditions are more common. Refractivity retrievals are broadly consistent between 10 and 35 km, with mean biases generally below 1%, whereas larger inter-mission differences occur in the lower troposphere and at upper levels. Missions with relatively few valid profiles also exhibit greater statistical uncertainty. Multi-mission applications should therefore consider both sampling complementarity and mission-specific retrieval accuracy when developing quality-control and observation-weighting strategies. Because the present analysis covers only seven days and the 6 h assessment is based on four windows from a single day, the results represent a short-term observational snapshot. Future work should extend the analysis to longer periods, quantify seasonal and regional variability, and evaluate optimized mission combinations in numerical weather prediction and climate applications.

**Code and data availability**

The radio occultation datasets used in this study were obtained from the National Meteorological Information Center of the China Meteorological Administration, comprising (1) global atmospheric profiles acquired under the WMO Global Telecommunication System (GTS) exchange agreement and subject to WMO data sharing and exchange policies, and (2) operational RO products from the commercial small-satellite constellations “Tanmu-1” and “Yunyao-1”, both of which have been admitted into the CMA integrated observation system in accordance with the Administrative Measures for the Admission and Exit of Meteorological Data Products and processed via the Tianqing meteorological big data cloud platform; these data are further governed by the CMA License Agreement for the Use of Meteorological Data, WMO GTS distribution rules, and the intellectual property clauses of the respective commercial satellite operators, meaning the authors are not authorized to redistribute them, and eligible researchers may register at data.cma.cn, sign the required license agreement, and apply for access. The code developed in this study is archived at Zenodo repository under DOI: 21866427. Access is currently restricted as the code forms part of an ongoing follow-up research project. The full codebase will be made publicly accessible under the same DOI upon completion of the related series of studies, estimated by 1 year. In the meantime, the code is available from the corresponding author upon reasonable request.

## Author contributions

LWQ and CR contributed equally to the conceptualization, methodology, formal analysis, visualization, and preparation of the original draft. XN and MXG contributed to the conceptualization, supervision, and project administration. LM, XL, LY and GP contributed to data curation and validation. YGL, HXQ, ZXG, and SYQ contributed to the interpretation of the results and the review and editing of the manuscript. All authors discussed the results and approved the final manuscript.

## Competing interests

The authors declare that they have no conflict of interest.

## Acknowledgements

We thank all individuals who contributed to this study. We are grateful to the European Centre for Medium-Range Weather Forecasts (ECMWF) for providing the ERA5 reanalysis data, and to the National Meteorological Information Center, China Meteorological Administration (CMA), for supplying the radio occultation data.

## Financial support

This research was funded by the National Natural Science Foundation of China (grant nos. U2542214 and U2442216).

## References

Anthes, R. A., Bernhardt, P. A., Chen, Y., Cucurull, L., Dymond, K. F., Ector, D., Healy, S. B., Ho, S.-P., Hunt, D. C., Kuo, Y.-H., Liu, H., Manning, K., McCormick, C., Meehan, T. K., Randel, W. J., Rocken, C., Schreiner, W. S., Sokolovskiy, S. V., Syndergaard, S., Thompson, D. C., Trenberth, K. E., Wee, T.-K., Yen,

N. L., and Zeng, Z.: The COSMIC/FORMOSAT-3 Mission: Early Results, Bulletin of the American Meteorological Society, 89, 313–334, https://doi.org/10.1175/BAMS-89-3-313, 2008.

Bai, W. H., Sun, Y. Q., Du, Q. F., Yang, G. L., Yang, Z. D., Zhang, P., Bi, Y. M., Wang, X. Y., Cheng, C., and Han, Y.: An introduction to the FY3 GNOS instrument and mountain-top tests, Atmos. Meas. Tech., 7, 1817–1823, https://doi.org/10.5194/amt-7-1817-2014, 2014.

Beyerle, G., Schmidt, T., Michalak, G., Heise, S., Wickert, J., and Reigber, C.: GPS radio occultation with GRACE: Atmospheric profiling utilizing the zero difference technique, Geophysical Research Letters, 32, https://doi.org/10.1029/2005GL023109, 2005.

Bonnedal, M., Christensen, J., Carlström, A., and Berg, A.: Metop-GRAS in-orbit instrument performance, GPS Solutions, 14, 109–120, https://doi.org/10.1007/s10291-009-0142-3, 2010.

Donlon, C. J., Cullen, R., Giulicchi, L., Vuilleumier, P., Francis, C. R., Kuschnerus, M., Simpson, W., Bouridah, A., Caleno, M., Bertoni, R., Rancaño, J., Pourier, E., Hyslop, A., Mulcahy, J., Knockaert, R., Hunter, C., Webb, A., Fornari, M., Vaze, P., Brown, S., Willis, J., Desai, S., Desjonqueres, J.-D., Scharroo, R., Martin-Puig, C., Leuliette, E., Egido, A., Smith, W. H. F., Bonnefond, P., Le Gac, S., Picot, N., and Tavernier, G.: The Copernicus Sentinel-6 mission: Enhanced continuity of satellite sea level measurements from space, Remote Sensing of Environment, 258, 112395, https://doi.org/10.1016/j.rse.2021.112395, 2021.

Du, Q., Liu, C., Li, W., Liu, C., Li, F., Qiao, H., Sun, Y., Bai, W., Wang, X., Wang, D., Meng, X., Cai, Y., Xia, J., and Wu, C.: The On-Orbit Performance of FY-3D GNOS, IGARSS 2019 - 2019 IEEE International Geoscience and Remote Sensing Symposium, 7669–7671, https://doi.org/10.1109/IGARSS.2019.8898370, 2019.

Faller, N., Weber, M., and GmbH, I.: TerraSAR-X and TanDEM-X: Revolution in spaceborne radar, 2007 IEEE International Geoscience and Remote Sensing Symposium, 23–28 July 2007, 4924–4928, 10.1109/IGARSS.2007.4423966,

Fjeldbo, G., Kliore, A. J., and Eshleman, V. R.: The Neutral Atmosphere of Venus as Studied with the Mariner V Radio Occultation Experiments, The Astronomical Journal, 76, 123, https://doi.org/10.1086/111096, 1971.

Fu, N. and Li, F.: An Introduction of GNSS Reflectometer Remote Sensing Mission From Yunyao Aerospace Technology Co., Ltd, 2021 IEEE Specialist Meeting on Reflectometry using GNSS and other Signals of Opportunity (GNSS+R), 14–17 Sept. 2021, 77–81, https://doi.org/10.1109/GNSSR53802.2021.9617716,

Ho, S., Hunt, D., Steiner, A., Mannucci, A., Kirchengast, G., Gleisner, H., Heise, S., von Engeln, A., Marquardt, C., Sokolovskiy, S., Schreiner, W., Scherllin-Pirscher, B., Ao, C., Wickert, J., Syndergaard, S., Lauritsen, K., Leroy, S., Kursinski, E., Kuo, Y., Foelsche, U., Schmidt, T., and Gorbunov, M.: Reproducibility of GPS radio occultation data for climate monitoring: Profile-to-profile inter-comparison of CHAMP climate records 2002 to 2008 from six data centers, Journal of Geophysical Research-Atmospheres, 117, https://doi.org/10.1029/2012jd017665, 2012.

Jaeggi, A., Arnold, D., Weiss, J., and Hunt, D.: Assessment of COSMIC-2 reduced-dynamic and kinematic orbit determination, EGU General Assembly Conference Abstracts, April 01, 2021, https://doi.org/10.5194/egusphere-egu21-12027, 2021.

Kornfeld, R., Arnold, B., Gross, M., Dahya, N., Klipstein, W., Gath, P., and Bettadpur, S.: GRACE-FO: The Gravity Recovery and Climate Experiment Follow-On Mission, Journal of Spacecraft and Rockets, 56, 931–951, https://doi.org/10.2514/1.A34326, 2019.

Kursinski, E. R., Hajj, G. A., Schofield, J. T., Linfield, R. P., and Hardy, K. R.: Observing Earth's atmosphere with radio occultation measurements using the Global Positioning System, Journal of Geophysical Research: Atmospheres, 102, 23429–23465, https://doi.org/10.1029/97JD01569, 1997.

https://doi.org/10.5194/egusphere-2026-4663
Preprint. Discussion started: 10 August 2026


Li, J., Lu, C., Zheng, Y., Ban, W., and Zhang, X.: Quality Assessment and Assimilation of Tianmu-1 GNSS Radio Occultation Refractivity Observations: A Preliminary Study, IEEE Transactions on Geoscience and Remote Sensing, 63, 1–17, https://doi.org/10.1109/TGRS.2025.3615559, 2025.

Masters, D., Duly, T., Esterhuizen, S., Irisov, V. G., Jales, P., Nguyễn, V., Nogués-Correig, O., Tan, L., Yuasa, T., and Angling, M.: Status and accomplishments of the Spire Earth observing nanosatellite constellation, 27 pp., https://doi.org/10.1117/12.2574110, 2020.

Miao, S., Sun, K., Hu, X., Chen, Y., Lv, F., Wang, J., Li, W., Wang, L., Wei, J., and Li, W.: On-Orbit Radiometric Performance Assessment of FY-3F MERSI-III: A Cross-Platform Intercomparison Approach Based on Global Pseudo-Invariant Pixels, IEEE Journal of Selected Topics in Applied Earth Observations and Remote Sensing, 18, 21514–21531, https://doi.org/10.1109/jstars.2025.3597457, 2025.

Padullés, R., Cardellach, E., Paz, A., Oliveras, S., Hunt, D. C., Sokolovskiy, S., Weiss, J. P., Wang, K. N., Turk, F. J., Ao, C. O., and de la Torre Juárez, M.: The PAZ polarimetric radio occultation research dataset for scientific applications, Earth Syst. Sci. Data, 16, 5643–5663, https://doi.org/10.5194/essd-16-5643-2024, 2024.

Paolella, S., Von Engeln, A., Padovan, S., Notarpietro, R., Marquardt, C., Sancho, F., Rivas Boscan, V., Morew, N., and Martin Alemany, F.: Assessment of operational non-time-critical Sentinel-6A Michael Freilich radio occultation data: insights into tropospheric GNSS signal cut-off strategies and processor improvements, Atmos. Meas. Tech., 18, 2825–2846, https://doi.org/10.5194/amt-18-2825-2025, 2025.

Righetti, P. L., de Juana Gamo, J. M., and Sancho, F.: Metop-C deployment and start of three-satellite operations, The Aeronautical Journal, 124, 902–916, https://doi.org/10.1017/aer.2020.10, 2020.

Rocken, C., Anthes, R., Exner, M., Hunt, D., Sokolovskiy, S., Ware, R., Gorbunov, M., Schreiner, W., Feng, D., Herman, B., Kuo, Y.-H., and Zou, X.: Analysis and validation of GPS/MET data in the neutral atmosphere, Journal of Geophysical Research: Atmospheres, 102, 29849–29866, https://doi.org/10.1029/97JD02400, 1997.

Roh, K.-M. and Hwang, Y.: Performance Comparison of KOMPSAT-5 Precision Orbit Determination with GRACE, International Journal of Aerospace Engineering, 2020, 7358286, https://doi.org/10.1155/2020/7358286, 2020.

Schmidt, D., Schreiner, P., Iijima, B., and Ao, C.: GRACE-FO radio occultation data processing – First result, https://doi.org/10.5194/gstm2020-76, 2020.

Schreiner, W. S., Weiss, J. P., Anthes, R. A., Braun, J., Chu, V., Fong, J., Hunt, D., Kuo, Y.-H., Meehan, T., Serafino, W., Sjoberg, J., Sokolovskiy, S., Talaat, E., Wee, T. K., and Zeng, Z.: COSMIC-2 Radio Occultation Constellation: First Results, Geophysical Research Letters, 47, e2019GL086841, https://doi.org/10.1029/2019GL086841, 2020.

Smith, E. K. and Weintraub, S.: The Constants in the Equation for Atmospheric Refractive Index at Radio Frequencies, Proceedings of the IRE, 41, 1035–1037, https://doi.org/10.1109/JRPROC.1953.274297, 1953.

Wickert, J., Reigber, C., Beyerle, G., König, R., Marquardt, C., Schmidt, T., Grunwaldt, L., Galas, R., Meehan, T. K., Melbourne, W. G., and Hocke, K.: Atmosphere sounding by GPS radio occultation: First results from CHAMP, Geophysical Research Letters, 28, 3263–3266, https://doi.org/10.1029/2001GL013117, 2001.

Xu, X., Han, W., Wang, J., Gao, Z., Li, F., Cheng, Y., and Fu, N.: Quality assessment of YUNYAO radio occultation data in the neutral atmosphere, Atmos. Meas. Tech., 18, 1339–1353, https://doi.org/10.5194/amt-18-1339-2025, 2025.

Zhang, P., Gu, S., Chen, L., Shang, J., Lin, M., Zhu, A., Yin, H., Wu, Q., Shou, Y., Sun, F., Xu, H., Yang, G., Wang, H., Li, L., Zhang, H., Chen, S., and Lu, N.: FY-3G Satellite Instruments and Precipitation Products: First Report of China's Fengyun Rainfall Mission In-Orbit, Journal of Remote Sensing, 3, 0097, https://doi.org/10.34133/remotesensing.0097, 2023.

https://doi.org/10.5194/egusphere-2026-4663
Preprint. Discussion started: 10 August 2026


Zhran, M., Mousa, A., Wang, Y., Hasher, F. F. B., and Jin, S.: Assessment of Commercial GNSS Radio Occultation Performance from PlanetiQ Mission, Remote Sensing, 16, 3339, https://doi.org/10.3390/rs16173339, 2024.